The Cryosphere

Impact of atmospheric forcing uncertainties on Arctic and Antarctic sea ice simulations in CMIP6 OMIP models

Xia Lin[1,2], François Massonnet[1], Thierry Fichefet[1], and Martin Vancoppenolle[3]

[1]Earth and Life Institute, Université catholique de Louvain, Louvain-la-Neuve, 1348, Belgium
[2]Southern Marine Science and Engineering Guangdong Laboratory (Zhuhai), Zhuhai, 519000, China
[3]Laboratoire d'Océanographie et du Climat, CNRS/IRD/MNHN, Sorbonne Université, 75252, Paris, France

Correspondence: Xia Lin (xia.lin@uclouvain.be)

Abstract. Atmospheric reanalyses are valuable datasets for driving ocean–sea ice general circulation models and for proposing multidecadal reconstructions of the ocean–sea ice system in polar regions. However, these reanalyses exhibit biases in these regions. It was previously found that the representation of Arctic and Antarctic sea ice in models participating in the Ocean Model Intercomparison Project Phase 2 (OMIP2, using the updated Japanese 55-year atmospheric reanalysis, JRA55-do) was significantly more realistic than in OMIP1 (forced by the atmospheric state from the Coordinated Ocean-ice Reference Experiments version 2, CORE-II). To understand why, we study the sea ice concentration budget and its relations to surface heat and momentum fluxes as well as the connections between the simulated ice drift and the ice concentration, the ice thickness and the wind stress in a subset of three models (CMCC-CM2-SR5, MRI-ESM2-0 and NorESM2-LM). These three models are representative of the ensemble and are the only ones to provide the surface fluxes and the tendencies of ice concentrations attributed to dynamic and thermodynamic processes required for the ice concentration budget analysis. The sea ice simulations of two other models (EC-Earth3 and MIROC6) forced by both CORE-II and JRA55-do reanalysis are also included in the analysis. It is found that negative summer biases in high-ice-concentration regions and positive biases in the Canadian Arctic Archipelago (CAA) and central Weddell Sea (CWS) regions are reduced from OMIP1 to OMIP2 due to surface heat flux changes. Net shortwave radiation fluxes provide key improvements in the Arctic interior, CAA and CWS regions. There is also an influence of improved surface wind stress in OMIP2 giving better winter Antarctic ice concentration and

the Arctic ice drift magnitude simulations near the ice edge. The ice velocity direction simulations in the Beaufort Gyre and the Pacific and Atlantic sectors of the Southern Ocean in OMIP2 are also improved owing to surface wind stress changes. This study provides clues on how improved atmospheric reanalysis products influence sea ice simulations. Our findings suggest that attention should be paid to the radiation fluxes and winds in atmospheric reanalyses in polar regions.

1 Introduction

Sea ice is an important component of the polar climate system. At high latitudes, the presence of sea ice affects the exchanges of heat, momentum and freshwater fluxes between the atmosphere and the ocean. Sea ice has experienced dramatic changes during recent decades, especially in the Arctic, where the total sea ice extent dramatically decreased over the satellite-observing period (Comiso et al., 2008; Stroeve and Notz, 2018). In the Antarctic, the total sea ice extent increased slightly, but statistically significantly, to a record high in 2014 and decreased dramatically to the lowest value in 2017 over the satellite record (Parkinson, 2019; Fogt et al., 2022). A record low sea ice extent was set in 2022 (Raphael and Handcock, 2022). Sea ice variability can drive changes in the atmospheric energy budget and circulation (Krikken and Hazeleger, 2015; Smith et al., 2017, 2022) as well as surface fluxes into the ocean and ocean circulation (Haumann et al., 2016; Sévellec et al., 2017; Meneghello et al., 2018).

A good simulation of sea ice is crucial for improving model predictions and climate change projections. However, limitations still exist in both fully coupled climate models and ocean–sea ice models. For the Arctic, the observed decline in sea ice cover lies within the spread of modeled trends, but the multimodel mean trend is underestimated in the third, fifth and sixth phases of the Coupled Model Intercomparison Project (CMIP, Stroeve et al., 2007; Massonnet et al., 2012; Rosenblum and Eisenman, 2017; Notz and SIMIP Community, 2020). The observed accelerated ice drift speed is not captured in CMIP3 models (Rampal et al., 2011), while the accelerated ice drift speed is produced in winter but not in summer in CMIP5 models (Tandon et al., 2018). Large ice edge and thickness errors in Arctic subregions are identified from the spatial distribution of sea ice in CMIP6 models (Stroeve et al., 2014; Watts et al., 2021). For the Antarctic, the CMIP5 and CMIP6 models fail to capture the slight increase in observed ice extent from 1979 to 2015, and they do not properly simulate the mean state and interannual variability of the ice cover (Mahlstein et al., 2013; Turner et al., 2013; Zunz et al., 2013; Shu et al., 2015, 2020; Roach et al., 2020). Large biases are also noticed in simulations conducted with ocean–sea ice models driven by atmospheric reanalysis data, in particular on the Antarctic sea ice extent variability and the ice thickness and motion in both hemispheres (e.g., Massonnet et al., 2011; Lecomte et al., 2016; Chevallier et al., 2017). By performing sensitivity experiments with these ocean–sea ice models, one can gain some insight into the origins of those biases. The focus of the present study is on quantifying and understanding how the sea ice simulation can be improved by changing atmospheric forcing fields in ocean–sea ice models.

Atmospheric reanalyses are particularly valuable in polar regions where in situ observations are scarce. However, these reanalyses have their limitations and biases (e.g., Lindsay et al., 2014; Bromwich et al., 2016; Barthélemy et al., 2018; Lin et al., 2018). Previous studies have shown that differences in the atmospheric forcing fields can affect the ocean–sea ice model simulations of the Arctic monthly mean sea ice thickness and total sea ice volume (e.g., Hunke and Holland, 2007; Lindsay et al., 2014; Sterlin et al., 2021), the Arctic and Antarctic sea ice concentration in the marginal ice zones (Chaudhuri et al., 2016) and the Antarctic sea ice extent, motion and thickness (Barthélemy et al., 2018). Wu et al. (2020) also showed the positive impacts of high-frequency (hourly to daily) atmospheric fluctuations on the Antarctic sea ice simulation, which implies that driving an ocean–sea ice model with a reanalysis that is developed at enhanced temporal and spatial resolution can help capture the small-scale atmospheric processes and eventually improve the representation of sea ice.

The CMIP6 Ocean Model Intercomparison Project (OMIP, Griffies et al., 2016) provides global ocean–sea ice model simulations in two streams of model experiments: OMIP1, forced by the Coordinated Ocean-ice Reference Experiments, version 2 interannual dataset (CORE-II; Large and Yeager, 2009), and OMIP2, forced by the updated Japanese 55-year atmospheric reanalysis (JRA55-do; Tsujino et al., 2018). The design of the CMIP6 OMIP simulations has been coordinated by the World Climate Research Programme (WCRP) Climate Variability and Predictability (CLIVAR) Working Group on Ocean Model Development Panel (OMDP), and ongoing research collaboration is done through the OMDP to further develop OMIP2 (Griffies et al., 2016). The same configuration is used under two different atmospheric forcing datasets as mentioned in Tsujino et al. (2020). The JRA55-do atmospheric forcing is relatively new with major improvements, e.g., increased temporal frequency (3 h) and horizontal resolution (0.5625°), compared to CORE-II forcing (6 h and 1.875°). The Arctic and Antarctic sea ice concentration and drift simulations in CMIP6 OMIP2 models forced by JRA55-do are improved compared to those in OMIP1 models forced by CORE-II (Tsujino et al., 2020; Lin et al., 2021). This provides an opportunity to check the processes contributing to these improvements under changed atmospheric forcing in the OMIP models and to compare the sea ice simulation differences in the Arctic and Antarctic.

The spatial variability of sea ice concentration and its links with the atmospheric circulation vary with season. The change in the position and strength of the cyclonic or anticyclonic circulation center over the sea ice can affect the sea ice motion and freezing/melting processes (Rigor et al., 2002; Raphael and Hobbs, 2014; Ding et al., 2017). Strong winter wind-driven ice exports in the Eurasian coastal region occur during high North Atlantic Oscillation (NAO) index years, which can have contributed to the reduction in summer Arctic sea ice extent observed during the 1980s and 1990s (Hu et al., 2002). In the Antarctic, the decreases in sea ice concentration generally occur in regions of poleward atmospheric flow, and the increases in sea ice concentration occur in regions of equatorward flow (Renwick et al., 2012). During the seasonal sea ice advance and retreat periods, the spatial ice concentration variability is associated with different atmospheric circulation patterns, and both thermal advection and dynamical forcing are important (Raphael and Hobbs, 2014). The thermodynamic and dynamic processes that contribute to the Antarctic sea ice concentration seasonal evolution are discussed in Barthélemy et al. (2018). These authors conducted three sensitivity experiments with different atmospheric forcing fields using the NEMO-LIM3 ocean–sea ice model. They found that differences in the thermodynamic component of the forcing were mostly responsible for the differences in ice concentration simulated by the model experiments during the melting season, while during the ice-expansion period, both thermodynamic and dynamic components were important. The relationships between spatially averaged observed sea ice drift speed in the central Arctic and ice concentration, ice thickness and wind stress were investigated by Olason and Notz (2014). According to their results,

on the seasonal timescales, ice drift speed changes in the central Arctic are primarily attributable to the changes in the ice concentration from June to November and changes in the ice thickness when the ice concentration is high, i.e., from December to March. The relationships between Arctic sea ice drift speed, concentration and thickness are relatively well captured by the NEMO-LIM3 model (Docquier et al., 2017) and the coupled GFDL-ESM2G model (Eyring et al., 2020), with higher drift speed associated with lower concentration and thickness. In the Antarctic, away from the coastline, the mean ice drift is significantly correlated with the wind forcing in the Pacific and Atlantic sectors, with the spatially averaged vector correlation coefficient larger than 0.7 (Kimura, 2004; Holland and Kwok, 2012).

This paper complements a companion publication (Lin et al., 2021) that documents a new Sea Ice Evaluation Tool (SITool v1.0) and applies this tool to assess the sea ice simulations in CMIP6 OMIP models. In that study, the improved Arctic and Antarctic ice concentration and drift simulations in CMIP6 OMIP2 compared to OMIP1 were highlighted from performance metrics and diagnostic spatial maps. In the present study, the thermodynamic and dynamic processes that contribute to the improved ice concentration simulation in OMIP2 compared to OMIP1 are assessed. The related surface sensible and latent heat fluxes, net shortwave and longwave radiation fluxes and surface wind stress on sea ice are investigated to trace the origin of simulated sea ice differences back to the forcing datasets. Meanwhile, the sensitivity of ice drift simulation to the changes in ice concentration, ice thickness and surface wind stress is examined to help understand the factors responsible for improving the ice drift simulation. This paper is organized as follows. The CMIP6 OMIP models, observational references and atmospheric reanalysis data are described in Sect. 2. The sea ice concentration simulations and the effects of the thermodynamic and dynamic components of the atmospheric forcing are presented in Sect. 3.1. The ice drift simulation and the connections to ice concentration, ice thickness and wind stress are discussed in Sect. 3.2. Finally, in Sect. 4, conclusions and a discussion are provided. Appendix A presents some extra sea ice diagnostics.

2 Models, observational references and atmospheric reanalysis data

Five CMIP6 OMIP models have been forced by both CORE-II (OMIP1) and JRA55-do (OMIP2) reanalysis data so far, and they are marked as $<$ model name $+$ /C and /J $>$, such as CMCC-CM2-SR5/C and CMCC-CM2-SR5/J, respectively. Details of the CMIP6 OMIP models can be found in Sect. 2.2 of our previous paper (Lin et al., 2021). The sea ice components of five CMIP6 OMIP models are given in Table 1. Three of the five models (CMCC-CM2-SR5, MRI-ESM2-0 and NorESM2-LM) provide the tendencies of sea ice con-

centration attributed to dynamic vs. thermodynamic processes and surface wind stress on sea ice, while two of them (CMCC-CM2-SR5 and NorESM2-LM) provide surface heat fluxes (sensible and latent heat fluxes and downward/upward shortwave and longwave radiation fluxes). The outputs from the three model groups that provided sea ice concentration tendencies are chosen to study the sea ice concentration budget and the effects of atmospheric forcing changes on the representation of surface fluxes and sea ice state. The sea ice simulations of another two models (EC-Earth3 and MIROC6) are also included in the analysis. The cross-metric analysis in Sect. 3.4 of Lin et al. (2021) shows that NorESM2-LM/J is the best-performing model regarding ice concentration in both hemispheres but the worst-performing one for ice drift. For the sake of readability and to not overload the paper, the figures of the main text focus on this model. The other four models do not show fundamentally different behavior when the atmospheric forcing is changed, and the figures from these four models are available in Appendix A.

Two sets of observational references for the sea ice concentration, thickness and ice drift are used for comparison. The two sea ice concentration products are derived from the passive microwave data by using the NASA Team algorithm (NSIDC-0051, Cavalieri et al., 1996) and the European Organisation for the Exploitation of Meteorological Satellites (EUMETSAT) Ocean and Sea Ice Satellite Application Facility algorithm (OSI-450, Lavergne et al., 2019), respectively. The first observed ice thickness data are derived from the measurements of the ESA's Environmental Satellite (Envisat) radar altimeter (Guerreiro et al., 2017), and the second one is derived from measurements of NASA's Ice, Cloud, and land Elevation Satellite (ICESat) Geoscience Laser Altimeter System (GLAS) (Yi and Zwally, 2009; Kurtz and Markus, 2012). The first observed ice drift product is processed by the NSIDC and enhanced by the Integrated Climate Data Center (ICDC-NSIDCv4.1, Tschudi et al., 2019), and the second ice drift data (KIMURA) are processed by Kimura et al. (2013). More information on the observational references can be found in Sect. 2.2 of Lin et al. (2021). The evaluation period is chosen according to available historical model outputs and observations and is consistent with the analysis in Lin et al. (2021). The ice concentrations, concentration tendencies and their relations to surface heat fluxes and wind stress are evaluated from 1980 to 2007, while the ice drift and its links to the ice concentration, ice thickness and wind stress are assessed from 2003 to 2007.

The monthly mean surface air temperature, specific humidity, downward shortwave and longwave radiation fluxes and wind speed in the CORE-II and JRA55-do reanalysis datasets from 1980 to 2007 are used to evaluate the differences between two forcing datasets.

Table 1. The details of the five CMIP6 OMIP sea ice models evaluated in the study. Some information can be found at the following link: https://www.cen.uni-hamburg.de/en/icdc/data/cryosphere/cmip6-sea-ice-area.html (last access: 3 April 2023).

Model	Sea ice model	Sea ice component	References
CMCC-CM2-SR5	CICE4	– Energy-conserving thermodynamics on one layer of snow and four layers of ice – Elastic–viscous–plastic (EVP) rheology – Ice thickness distribution (ITD) with five thickness categories – A delta-Eddington multiple-scattering shortwave radiation treatment – Explicit level-ice melt pond parameterization	Hunke and Lipscomb (2008); Cherchi et al. (2019).
EC-Earth3	LIM3	– Energy-conserving halo thermodynamics with prognostic sea ice salinity on one layer of snow and two layers of ice – EVP – ITD with five thickness categories – Empirical albedo function, exponential attenuation of solar radiation in sea ice if no snow – Melt ponds: step reduction in albedo when $T_{su} = 0\,°C$	Rousset et al. (2015); Döscher et al. (2022).
MIROC6	COCO4.9	– Energy-conserving thermodynamics on zero layers of snow (without heat capacity) and one layer of ice – EVP – ITD with five thickness categories – Empirical albedo function – Implicit melt ponds	Komuro et al. (2012); Tatebe et al. (2019).
MRI-ESM2-0	MRI.COM4.4	– Energy-conserving thermodynamics following Mellor and Kantha (1989) on zero layers of snow and one layer of ice – EVP – ITD with five thickness categories – The "default" CICE CCSM3 radiation scheme – Implicit melt ponds: adjust the albedo based on surface conditions	Tsujino et al. (2010); Hunke et al. (2015); Yukimoto et al. (2019).
NorESM2-LM	CICE5.1.2	– Mushy-layer thermodynamics with prognostic sea ice salinity on three layers of snow and eight layers of ice – EVP – ITD with five thickness categories – A delta-Eddington multiple-scattering shortwave radiation treatment – Explicit level-ice melt pond parameterization	Hunke et al. (2015); Seland et al. (2020).

3   Results

3.1   Sea ice concentration

The 1980–2007 September and February mean spatial distributions of the Arctic and Antarctic sea ice concentrations from the NorESM2-LM simulations and observational reference OSI-450 compared to the observational reference NSIDC-0051 are shown in Fig. 1, and figures from CMCC-SR5-CM2, MRI-ESM2-0, EC-Earth3 and MIROC6 are displayed in Figs. A1 and A2. The model biases are much larger than observational differences (Fig. 1, second column). Olason and Notz (2014) suggested that, for concentrations above 80 %, variations in sea ice state variables (concentration and thickness) greatly affect the ice drift speed. To study the drivers of the ice concentration and drift speed changes, we divided the regions into two parts for each month, with ice concentration larger (interior) and smaller (exterior) than

80 % in the NSIDC-0051 observational reference. The black lines in Fig. 1 exhibit September and February contours of 80 % concentration in the NSIDC-0051 data. Spatial averages of the 1980–2007 September and February mean sea ice concentration biases are given in Tables 2 and 3 for the Arctic and Antarctic, respectively. The spatial averages over the interior and exterior regions are calculated with data closer than 75 km to the coast removed to reduce the spatial noise.

By applying the mean ice concentration difference metric developed in Lin et al. (2021), one finds that the Arctic mean ice concentration biases in OMIP1 simulations from 1980 to 2007 are reduced in OMIP2. The improvements are primarily in the boreal summer in the interior region and the Canadian Arctic Archipelago (CAA) region as shown in Figs. 1, A1 and A2. In September, the ice concentration is primarily underestimated in the interior region and overestimated in the CAA region in OMIP1 simulations, and those biases are re-

Table 2. Spatial averages of the 1980–2007 September mean Arctic sea ice concentration (SIC) biases (vs. NSIDC-0051, Figs. 1, A1 and A2), ice concentration tendencies through thermodynamic and dynamic processes (Figs. 2, 3, A3 and A4) and surface heat fluxes and surface stress on sea ice (Figs. 4 and A5) over March–August. The results derived from five model groups under the OMIP1 (/C) and OMIP2 (/J) runs are listed. The spatial averages over the interior region in the Arctic and the Canadian Arctic Archipelago (CAA) in summer are given. The improvements in ice concentration simulations and the contributions from the thermodynamic process and the surface heat flux to sea ice are marked in bold for the interior region and the CAA region.

			Arctic				
Variables	Periods	Regions	NorESM2-LM/C (/J)	CMCC-SR5-CM2/C (/J)	MRI-ESM2-0/C (/J)	EC-Earth3/C (/J)	MIROC6/C (/J)
SIC bias	Sep	**Interior**	**−0.31[0.02]**	**−0.52[−0.16]**	−0.03[0.06]	−0.04[0.04]	**−0.07[−0.01]**
		CAA	**0.26[0.07]**	**0.10[−0.03]**	**0.13[0.01]**	0.32[0.18]	0.29[0.27]
siconc tendency thermo. ($10^{-3}\,\mathrm{d}^{-1}$)	Mar–Aug	**Interior**	**−2.2[0.6]**	**−3.2[−0.9]**	0.4[1.5]	/	
		CAA	**−0.05[−1.05]**	**−0.7[−1.4]**	**1.0[0.22]**		
siconc tendency dyn. ($10^{-3}\,\mathrm{d}^{-1}$)	Mar–Aug	Interior	−1.6[−1.9]	−1.4[−1.6]	−2.0[−2.2]		
		CAA	−1.6[−1.7]	−1.6[−1.63]	−2.1[−2.19]		
Surface heat flux on sea ice (downward positive, $\mathrm{W\,m^{-2}}$)	Mar–Aug	**Interior**	**27.4[14]**	**32.9[19.1]**	/		
		CAA	**24.5[40.2]**	**28.7[46.2]**	/		
Surface stress on sea ice ($10^{-3}\,\mathrm{N\,m^{-2}}$)	Mar–Aug	Interior	11.9[12.6]	11.5[12.3]	12.2[12.6]		
		CAA	16.6[16.8]	17.4[18.9]	19.8[20.3]		

Table 3. Spatial averages of the 1980–2007 February and September mean Antarctic SIC biases (vs. NSIDC-0051, Figs. 1, A1 and A2), the ice concentration tendencies through thermodynamic and dynamic processes (Figs. 2, 3, A3 and A4) and surface heat fluxes and surface stress on sea ice (Figs. 4 and A5) over October–January and March–August. The results derived from five model groups under the OMIP1 (/C) and OMIP2 (/J) runs are listed. The spatial averages over the interior region in the Antarctic (52 to 60° W) and central Weddell Sea (CWS) in summer and over the exterior region in the Antarctic (70 to 180° E) in winter are given. The improvements in ice concentration simulations and the contributions from thermodynamic processes and the surface heat flux on sea ice are marked in bold for the interior region and the CWS region. The improvements in ice concentration simulations of the exterior region and the contributions from dynamic processes and the surface stress on sea ice are marked in bold italic.

			Antarctic				
Variables	Periods	Regions	NorESM2-LM/C (/J)	CMCC-SR5-CM2/C (/J)	MRI-ESM2-0/C (/J)	EC-Earth3/C (/J)	MIROC6/C (/J)
SIC bias	Feb	**Interior**	**−0.71[−0.41]**	**−0.68[−0.51]**	**−0.84[−0.76]**	**−0.66[−0.54]**	**−0.87[−0.60]**
		CWS	0.005[0.003]	**0.36[0.22]**	**0.08[0.01]**	0.023[−0.0003]	−0.0003[−0.0003]
	Sep	***Exterior***	*0.24[0.09]*	*0.19[0.1]*	*0.33[0.2]*	*0.3[0.21]*	*0.2[0.11]*
siconc tendency thermo. ($10^{-3}\,\mathrm{d}^{-1}$)	Oct–Jan	**Interior**	**−4.5[−1.9]**	**−5.2[−2.9]**	**−6.1[−3.9]**	/	
		CWS	−6.1[−6.12]	**−4.4[−7.2]**	**−3.0[−5.2]**		
	Mar–Aug	Exterior	1.1[2.7]	0.5[1.4]	3.1[4.2]		
siconc tendency dyn. ($10^{-3}\,\mathrm{d}^{-1}$)	Oct–Jan	Interior	−1.2[−2.1]	−0.3[−1.2]	−1.3[−3]		
		CWS	−1.3[−1.33]	−1.0[−0.2]	−3.7[−2.6]		
	Mar–Aug	***Exterior***	*2.9[0.5]*	*3.1[1.7]*	*1.2[−0.6]*		
Surface heat flux on sea ice (downward positive, $\mathrm{W\,m^{-2}}$)	Oct–Jan	**Interior**	**32.4[23.1]**	**31.6[27.8]**	/		
		CWS	7.1[26.3]	**4.6[34.1]**	/		
	Mar–Aug	Exterior	−19.5[−16.3]	−14.1[−6.5]	/		
Surface stress on sea ice ($10^{-3}\,\mathrm{N\,m^{-2}}$)	Oct–Jan	Interior	24.3[24.9]	24.6[25]	31.3[26.5]		
		CWS	26.8[25.3]	35.1[29.1]	41.9[39.6]		
	Mar–Aug	***Exterior***	*29.1[22.7]*	*20.4[18.5]*	*75.5[68.8]*		
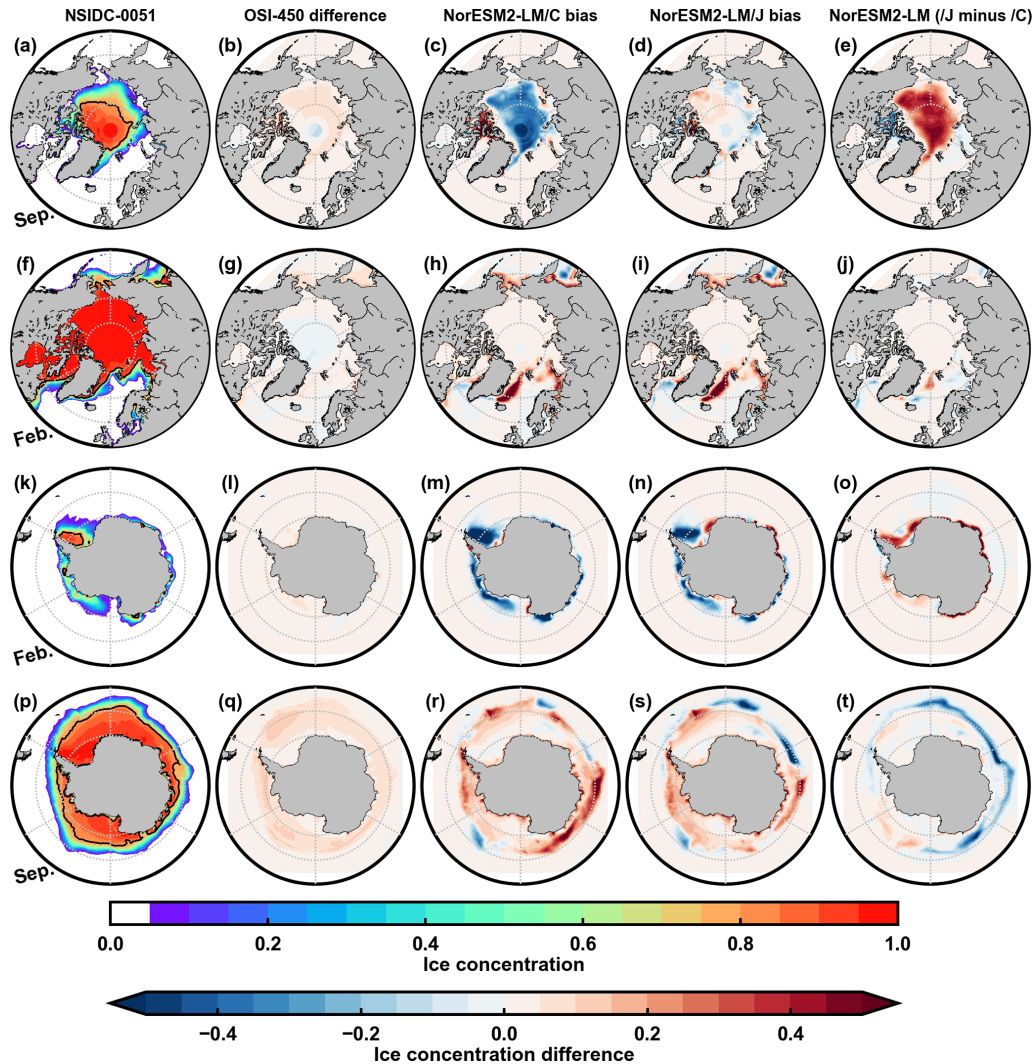
Figure 1. 1980–2007 September and February mean Arctic **(a–j)** and Antarctic **(k–t)** sea ice concentrations from the NSIDC-0051 data (first column) and the differences between OSI-450 and NSIDC-0051 (second column), NorESM2-LM/C and NSIDC-0051 (third column), NorESM2-LM/J and NSIDC-0051 (fourth column) and NorESM2-LM/J and NorESM2-LM/C (fifth column). The black lines are contours of 80 % concentration **(a, f, k, p)**, which delineate the interior and exterior domains to compute spatial averages in Tables 2 to 4.

duced in OMIP2 runs. The spatial mean ice concentration biases in the interior region are reduced from −0.31 to 0.02 in NorESM2-LM, from −0.52 to −0.16 in CMCC-SR5-CM2 and from −0.07 to −0.01 in MIROC6 by changing the atmospheric forcing from CORE-II to JRA55-do (Table 2). The reduced negative ice concentration biases in MRI-ESM2-0 and EC-Earth3 are over the eastern part of the central Arctic Ocean. The spatial mean ice concentration biases in the interior region in MRI-ESM2-0/C (−0.03) and EC-Earth3/C (−0.04) are not weakened in MRI-ESM2-0/J (0.06) and EC-Earth3/J (0.04). The spatial mean ice concentration biases in the CAA are reduced from 0.26 to 0.07 in NorESM2-LM, from 0.1 to −0.03 in CMCC-SR5-CM2, from 0.13 to 0.01 in MRI-ESM2-0, from 0.32 to 0.18 in EC-Earth3 and from 0.29 to 0.27 in MIROC6 under changed forcing from CORE-

II to JRA55-do. In February, the ice concentration biases in exterior regions in five OMIP1 simulations are also present in OMIP2 runs, with minor reductions.

The Antarctic mean ice concentration biases in OMIP1 simulations from 1980 to 2007 are also diminished. The improvements are mainly over the coastal regions of the western Weddell Sea and the Amundsen Sea in the austral summer and over exterior regions from 70 to 180° E in winter from OMIP1 to OMIP2 as shown in Figs. 1, A1 and A2. In February, the spatial mean ice concentration biases in the interior region from 52 to 60° W are reduced from −0.71 to −0.41 in NorESM2-LM, from −0.68 to −0.51 in CMCC-SR5-CM2, from −0.84 to −0.76 in MRI-ESM2-0, from −0.66 to −0.54 in EC-Earth3 and from −0.87 to −0.60 in MIROC6 by changing the atmospheric forcing from CORE-

II to JRA55-do (Table 3). Positive ice concentration biases are shown in the central Weddell Sea (CWS) in CMCC-SR5-CM2/C, MRI-ESM2-0/C and EC-Earth3/C but not in NorESM2-LM/C and MIROC6/C. The spatial mean ice concentration biases over the CWS are reduced from 0.36 to 0.22 in CMCC-SR5-CM2, from 0.08 to 0.01 in MRI-ESM2-0 and from 0.02 to −0.0003 in EC-Earth3 under changed forcing from CORE-II to JRA55-do. NorESM2-LM exhibits a larger positive bias on the East Antarctic coast when forced by JRA55-do as compared to CORE-II. In September, the spatial mean ice concentration biases in exterior regions from 70 to 180° E are reduced from 0.24 to 0.09 in NorESM2-LM, from 0.19 to 0.10 in CMCC-SR5-CM2, from 0.33 to 0.20 in MRI-ESM2-0, from 0.30 to 0.21 in EC-Earth3 and from 0.20 to 0.11 in MIROC6 under changed forcing from CORE-II to JRA55-do.

3.1.1 Effects of thermodynamic vs. dynamic processes on ice concentration tendencies

To understand the differences in the simulated sea ice concentration noted in Figs. 1, A1 and A2, we analyze the thermodynamic and dynamic processes contributing to the concentration tendencies during the melt and growth seasons under different atmospheric forcings (Figs. 2, 3, A3 and A4). The idea is close to the sea ice concentration budget proposed in Holland and Kwok (2012) and applied in Uotila et al. (2014), Lecomte et al. (2016) and Barthélemy et al. (2018). The contributing thermodynamic processes to the concentration tendencies are freezing or melting, whereas the relevant dynamic processes are ice advection, divergence/convergence and mechanical redistribution (rafting/ridging). The tendencies of ice concentration due to dynamic and thermodynamic processes are available as standard SIMIP diagnostics in the three models (Notz et al., 2016). Spatial averages of the Arctic and Antarctic ice concentration tendencies due to thermodynamic and dynamic processes are listed in Tables 2 and 3, respectively.

Compared to OMIP1 runs, changes in thermodynamic processes in the Arctic Ocean and the CAA region contribute to the ice concentration changes in OMIP2 runs during March to August (Figs. 2 and A3). The differences between OMIP1 and OMIP2 simulations in the contributions from dynamic processes are small. As shown in Table 2, the spatial mean ice concentration tendencies due to thermodynamic processes (10^{-3} d^{-1}) from OMIP1 to OMIP2 simulations are increased in the interior region (from −2.2 to 0.6 in NorESM2-LM and from −3.2 to −0.9 in CMCC-SR5-CM2) and decreased in the CAA (from −0.05 to −1.05 in NorESM2-LM, from −0.7 to −1.4 in CMCC-SR5-CM2 and from 1.0 to 0.22 in MRI-ESM2-0). This is consistent with the reduced September Arctic ice concentration biases in OMIP2 runs (Figs. 1c to e, A1a to f). That is, by changing the atmospheric forcing from CORE-II to JRA55-do, the simulations of Arctic summer ice concentration in the Arctic Ocean and
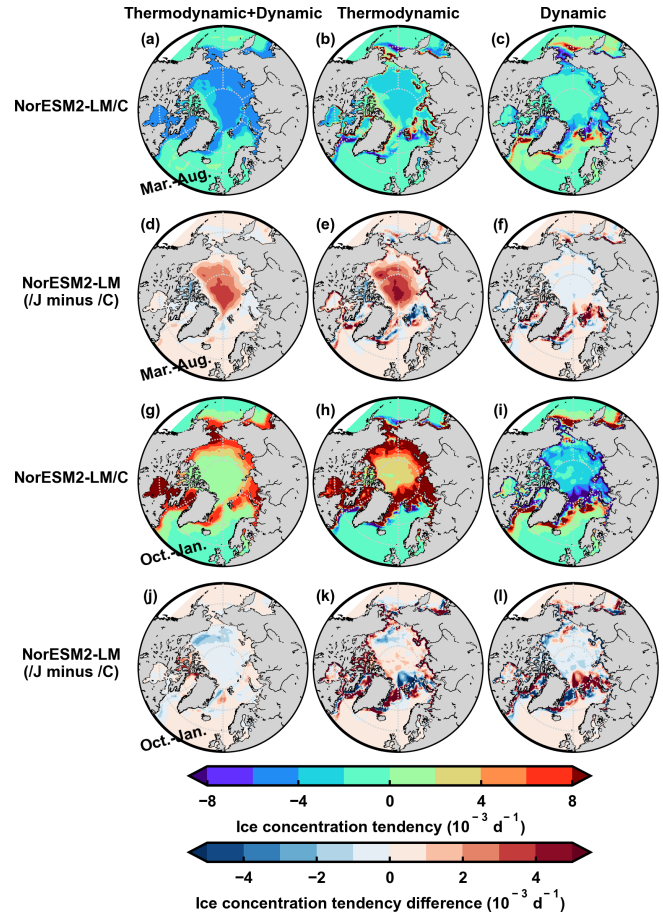
Figure 2. 1980–2007 March–August (**a–f**) and October–January (**g–l**) mean Arctic sea ice concentration tendencies in NorESM2-LM/C (**a–c, g–i**) and the differences between NorESM2-LM/J and NorESM2-LM/C (**d–f, j–l**). The ice concentration tendencies due to thermodynamic and dynamic processes in total are in the first column, and individual contributions are in the second and third columns.

the CAA region are improved owing to a better representation of the thermodynamic processes. The thermodynamic processes in MRI-ESM2-0/C contribute to the increase in ice concentration in the Beaufort Gyre region (Fig. A3e) but not the decrease in the other two models (Figs. 2b and A3b) during March to August. This explains why the large negative ice concentration biases in the Beaufort Gyre region in the other two models are not present in MRI-ESM2-0/C (Figs. 1c to e, A1a to f).

The major Arctic winter ice concentration biases are located in the exterior regions in OMIP1 simulations, with a minor reduction in OMIP2 runs (Figs. 1h to j and A1g to l). The winter ice concentration simulation in exterior regions is complicated because both dynamic and thermodynamic processes are important. The contributions from thermodynamic and dynamic processes are anticorrelated in these regions, with the dynamic processes increasing ice concen-
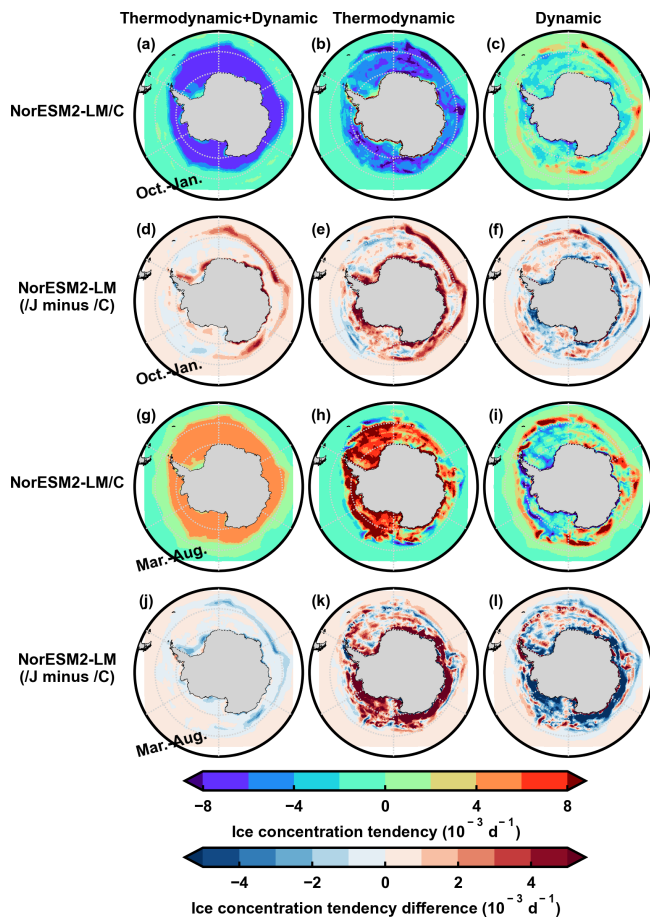
Figure 3. Same as Fig. 2 but for the 1980–2007 October–January (**a–f**) and March–August (**g–l**) mean Antarctic sea ice concentration tendencies.

tration through the expansion of sea ice and the thermodynamic processes contributing to ice melt. During October to January, the increased Arctic ice concentration is dominated by dynamic processes in exterior regions in OMIP1 simulations (Figs. 2 and A3). Compared to OMIP1 runs, these dynamic processes in OMIP2 runs contribute to the decreased ice concentration in exterior regions in the east of Greenland, while thermodynamic processes contribute to the increased ice concentration. This contributes to minor winter ice concentration differences between OMIP1 and OMIP2 simulations.

During October to January, the thermodynamic processes contribute to the decreased ice concentration in the Southern Ocean, except in some coastal regions, and the dynamic processes contribute to the decreased ice concentration in the inner region in the three OMIP1 runs (Figs. 3 and A4). Compared to the OMIP1 runs, the thermodynamic processes dominate the increased ice concentration in the coastal regions of the western Weddell Sea and Amundsen Sea in the three OMIP2 simulations and the decreased ice concentration in the CWS in CMCC-SR5-CM2/J and MRI-ESM2-

0/J. As shown in Table 3, the spatial mean ice concentration tendency due to thermodynamic processes ($10^{-3}\,\mathrm{d}^{-1}$) from OMIP1 to OMIP2 simulations is increased in the interior region from 52 to 60° W (from -4.5 to -1.9 in NorESM2-LM, from -5.2 to -2.9 in CMCC-SR5-CM2 and from -6.1 to -3.9 in MRI-ESM2-0) and decreased in the CWS (from -4.4 to -7.2 in CMCC-SR5-CM2 and from -3.0 to -5.2 in MRI-ESM2-0). This is consistent with the reduced February Antarctic ice concentration biases in OMIP2 runs (Figs. 1m to o, A1m to r). The positive bias in the coastal region of the East Antarctic sector in the NorESM2-LM/J simulation (Fig. 1n) is related to thermodynamic processes (Fig. 3e). By changing the atmospheric forcing from CORE-II to JRA55-do, the simulations of Antarctic summer ice concentration in the coastal regions of the western Weddell Sea and the Amundsen Sea as well as the CWS region are improved owing to the thermodynamic processes.

During March to August, the thermodynamic processes contribute to the increased Antarctic ice concentration, except for some exterior regions, and the dynamic processes contribute to the increased ice concentration primarily in the exterior region (Figs. 3 and A4). Compared to OMIP1 runs, the dynamic processes dominate the decreased ice concentration in exterior regions in the three OMIP2 simulations. As shown in Table 3, the spatial mean ice concentration tendencies related to dynamic processes ($10^{-3}\,\mathrm{d}^{-1}$) from OMIP1 to OMIP2 simulations are decreased in the exterior region from 70 to 180° E (from 2.9 to 0.5 in NorESM2-LM, from 3.1 to 1.7 in CMCC-SR5-CM2 and from 1.2 to -0.6 in MRI-ESM2-0). This is consistent with the reduced September Antarctic ice concentration biases from 70 to 180° E in OMIP2 runs (Figs. 1r to t, A1s to x). The simulations of the Antarctic winter ice concentration in the exterior region from 70 to 180° E are improved due to the dynamic processes when forced by JRA55-do as compared to CORE-II.

In general, by changing the atmospheric forcing from CORE-II to JRA55-do, the improvements in the simulation of summer Arctic and Antarctic sea ice concentrations within the pack are driven by differences in the thermodynamic tendency terms, while the improvements in Antarctic winter concentration simulation in the exterior region from 70 to 180° E are dominated by differences in dynamic tendency terms. For other cases (winter Arctic ice concentration in the exterior region, ice concentration in coastal regions), improvements are not as clear.

3.1.2 Surface heat and momentum flux

To trace the origin of the differences in thermodynamic and dynamic tendency terms noted in the previous section, the surface heat and momentum fluxes available from the standard OMIP1 and OMIP2 model outputs are compared. The sign convention for flux in this study is that a downward flux towards the surface is positive. The net surface heat flux is downward (positive) in the Arctic during March to August

and in the Antarctic during October to January in OMIP1 runs (Figs. 4 and A5). Compared to OMIP1 simulations, the net surface heat fluxes in OMIP2 simulations are smaller in the central Arctic Ocean and over the coastal regions of the western Weddell Sea and larger in the CAA and CWS regions. As shown in Tables 2 and 3, the spatial mean net surface heat flux from OMIP1 to OMIP2 simulations decreased in the Arctic interior region (from 27.4 to 14 W m^{-2} in NorESM2-LM and from 32.9 to 19.1 W m^{-2} in CMCC-SR5-CM2) and in the Antarctic interior region from 52 to 60° W (from 32.4 to 23.1 W m^{-2} in NorESM2-LM and from 31.6 to 27.8 W m^{-2} in CMCC-SR5-CM2) and increased in the CAA region (from 24.5 to 40.2 W m^{-2} in NorESM2-LM and from 28.7 to 46.2 W m^{-2} in CMCC-SR5-CM2) and the CWS region (4.6 to 34.1 W m^{-2} in CMCC-SR5-CM2). The net surface heat flux changes in OMIP2 simulations contribute to the improved ice concentration simulation in those regions (Figs. 1 and A1). The simulated surface fluxes on sea ice are compared to ERA5 reanalysis data, which is the fifth-generation ECMWF reanalysis for the global atmosphere, land surface and ocean waves (Hersbach et al., 2018). The net surface heat flux in OMIP2 simulations in these regions is close to the net surface heat flux on sea ice derived from ERA5 12-hourly data (not shown).

To study which part dominates the surface heat flux changes from OMIP1 to OMIP2 simulations, the surface sensible and latent heat fluxes and the net shortwave and longwave radiation fluxes are computed (Figs. 5 and A6). Compared to OMIP1 simulations, the net shortwave radiation flux and latent heat flux in OMIP2 are smaller in the central Arctic Ocean and the coastal region of the western Weddell Sea, the net shortwave radiation flux is larger in the CAA and CWS regions and the sensible heat flux is larger in the CAA region. As shown in Table 4, the decreased net shortwave radiation flux in OMIP2 simulations (-13.4 W m^{-2} in NorESM2-LM and -12.7 W m^{-2} in CMCC-SR5-CM2) dominates the net surface heat flux changes in the central Arctic Ocean. The decreased latent heat flux in OMIP2 simulations (-12.6 W m^{-2} in NorESM2-LM and -13.1 W m^{-2} in CMCC-SR5-CM2) dominates the net surface heat flux changes in the coastal region of the western Weddell Sea. In the CAA region, the increased sensible heat flux and net shortwave radiation flux in OMIP2 simulations (16.1 and 10.0 W m^{-2} in NorESM2-LM, 14.9 and 13.6 W m^{-2} in CMCC-SR5-CM2) dictate the net surface heat flux changes. In the CWS region, the increased net shortwave radiation flux (19.9 W m^{-2} in NorESM2-LM and 39.2 W m^{-2} in CMCC-SR5-CM2) is the major contributor to the net surface heat flux changes.

The changes in the shortwave radiation flux are crucial for the summer ice concentration changes in the OMIP2 simulations in the Arctic interior region and the CAA and CWS regions. The downward and upward shortwave radiation fluxes in NorESM2-LM and CMCC-SR5-CM2 (Fig. A7) and spatial averages (Table 4) are displayed. The decreased downward shortwave radiation flux in OMIP2 simulations

(-9.6 W m^{-2} in NorESM2-LM and -9.9 W m^{-2} in CMCC-SR5-CM2) is mostly responsible for the net shortwave radiation flux changes in the central Arctic Ocean. The increased net shortwave radiation fluxes in the CAA and CWS regions are related to the increased downward and decreased upward shortwave radiation flux in OMIP2 simulations.

Compared to other regions, the surface stress on ice along the eastern coasts of Greenland, Svalbard and Baffin Island, near the Bering Strait from 60 to 70° N, in the Antarctic coastal regions and inside the subpolar gyres is larger in OMIP1 simulations (third column in Fig. 4 and third and fifth columns in Fig. A5). This contributes to the smaller ice concentration due to the dynamic processes in those regions (Figs. 2, 3, A3 and A4). The large winter concentration biases in both hemispheres are located in exterior regions. In wintertime, the reduced Antarctic ice concentration biases in the exterior region from 70 to 180° E in OMIP2 simulations are dominated by the dynamic processes, as discussed in the previous section (Figs. 3 and A4). Compared to OMIP1 simulations, the surface wind stress on Antarctic sea ice in OMIP2 simulations is weaker in the inner part of the exterior region from 70 to 180° E (Figs. 4o and p, A5u to x). As shown in Table 3, the spatial mean surface wind stress on sea ice is decreased from OMIP1 to OMIP2 simulations in the exterior region from 70 to 180° E (from 29.1 to 22.7 N m^{-2} in NorESM2-LM, from 20.4 to 18.5 N m^{-2} in CMCC-SR5-CM2 and from 75.5 to 68.8 N m^{-2} in MRI-ESM2-0). The decreased surface wind stress in OMIP2 simulations in the inner part of the exterior region weakens the ice motion and reduces the ice concentration in the exterior region from 70 to 180° E. The surface wind stress in OMIP2 simulations in the inner part of the exterior region is close to the surface stress on sea ice derived from ERA5 hourly data (not shown).

The improvement in the winter Arctic ice concentration in the exterior region is not as clear. Compared to OMIP1 simulations, the surface wind stress in OMIP2 simulations is smaller along the eastern coasts of Greenland, Svalbard and Baffin Island (Figs. 4g and h, A5i to l). This is consistent with the decrease in ice concentration in the exterior region in OMIP2 simulations due to the dynamic processes away from the eastern coast (Figs. 2l, A3u and A3x). However, the thermodynamic processes in OMIP2 simulations contribute to the increase in ice concentration, which is close to the decrease due to the dynamic processes in these regions (Figs. 2k, A3t and A3w). The different contributions of the thermodynamic processes to the winter ice concentration tendency in the exterior region between OMIP1 and OMIP2 simulations are primarily related to the dynamic processes, while the surface heat flux difference on the sea ice is small.

To identify how the differences in the atmospheric forcings are transferred to the model results, the 1980–2007 mean surface air temperature, specific humidity, downward shortwave and longwave radiation fluxes during melting months and wind speed during freezing months in CORE-II and JRA55-
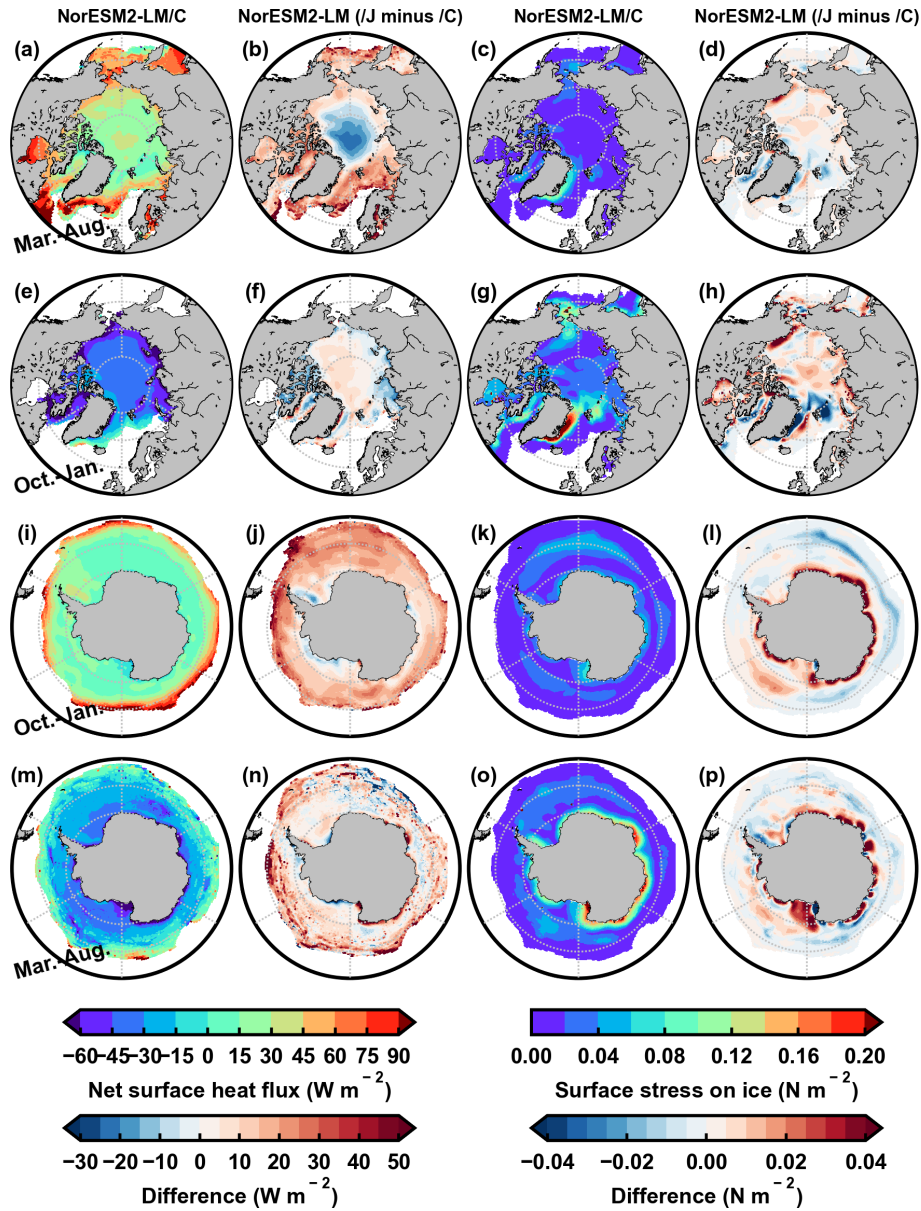
Figure 4. 1980–2007 March–August and October–January mean Arctic (**a–h**) and Antarctic (**i–p**) net surface heat flux (first two columns) and surface stress (last two columns) on sea ice. The positive values indicate a surface flux downward. The first and third columns correspond to NorESM2-LM/C, and the second and fourth columns are differences between NorESM2-LM/J and NorESM2-LM/C.

do are shown in Fig. 6. The selection to show these variables during melting/freezing months is because in general the ice concentration simulations are improved from OMIP1 to OMIP2 in summer due to surface heat flux changes and in winter due to wind stress changes. Compared to CORE-II, the downward shortwave radiation flux and specific humidity in the central Arctic Ocean (Fig. 6g and h) and specific humidity in the coastal region of the western Weddell Sea (Fig. 6q) in JRA5-do are smaller, the downward shortwave radiation flux in the CAA and CWS regions (Fig. 6h and r) and the air temperature in the CAA region are larger (Fig. 6f)

and the surface wind speed on Antarctic sea ice in the inner part of the exterior region from 70 to 180° E is weaker (Fig. 6t). These differences in the atmospheric forcing are transferred to the surface fluxes and contribute to the improved ice concentration simulation in those regions. Compared to OMIP1 simulations, the downward shortwave radiation flux and latent heat flux in the central Arctic Ocean and the latent heat flux in the coastal region of the western Weddell Sea in OMIP2 are smaller, the downward shortwave radiation flux in the CAA and CWS regions and the sensible heat flux in the CAA region are larger (Figs. 5, A6, A7, Ta-

Table 4. Spatial averages of the 1980–2007 mean Arctic (March–August) and Antarctic (October–January) net surface heat fluxes (Figs. 4 and A5), sensible and latent heat fluxes, net shortwave and longwave radiation fluxes (Figs. 5 and A6), downward and upward shortwave fluxes (Fig. A7) and downward and upward longwave fluxes over the interior region in the Arctic and Antarctic (52 to 60° W) and the CAA and CWS regions. The results derived from the two model groups under the OMIP1 (/C) and OMIP2 (/J) runs are listed. The contributions from the surface heat flux to the improved ice concentration simulations are marked in bold for the interior region and the CAA and CWS regions.

Periods and regions	Variables (W m^{-2}) downward positive	Arctic		Antarctic	
		NorESM2-LM /C [/J]	CMCC-SR5-CM2 /C [/J]	NorESM2-LM /C [/J]	CMCC-SR5-CM2 /C [/J]
Interior	Net surface heat flux	**27.4[14.0]**	**32.9[19.1]**	**32.4[23.1]**	**31.6[27.8]**
	Sensible	−7.0[3.9]	−6.9[3.4]	2.7[4.9]	5.4[6.5]
	Latent	4.8[−4.4]	4.6[−5.0]	**0.8[−11.8]**	**1.7[−11.4]**
	Net shortwave	**60.8[47.4]**	**66.4[53.7]**	71.5[67.3]	66.5[69.8]
	Downward shortwave / Upward shortwave	**177.7 [168.1]** / −116.9 [−120.7]	**178.8 [168.9]** / −112.5 [−115.3]	238.2 [238.7] / −166.6 [−171.3]	237.6 [238.2] / −171.1 [−168.4]
	Net longwave	−31.2[−32.9]	−31.2[−33.0]	−42.5[−37.3]	−41.9[−37]
	Downward longwave / Upward longwave	242.3 [238.4] / −273.4 [−271.2]	242.3 [238.6] / −273.5 [−271.6]	253.0 [251.0] / −295.5 [−288.3]	252.4 [250.4] / −294.3 [−287.4]
CAA/CWS	Net surface heat flux	**24.5[40.2]**	**28.7[46.2]**	**7.1[26.3]**	**4.6[34.1]**
	Sensible	**−6.6[9.5]**	**−5.6[9.3]**	8.5[8.4]	13.1[9.1]
	Latent	5.2[−1.7]	5.2[−2.2]	−10.5[−12.9]	−8.2[−13.3]
	Net shortwave	**53.6[63.6]**	**56.5[70.1]**	**46.2[66.1]**	**34.3[73.5]**
	Downward shortwave / Upward shortwave	172.7 [178.7] / −119.1 [−115.1]	173.3 [177.8] / −116.8 [−107.7]	215.0 [224.8] / −168.8 [−158.6]	213.5 [223.7] / −179.2 [−150.2]
	Net longwave	−27.7[−31.1]	−27.4[−30.9]	−37.1[−35.3]	−34.5[−35.2]
	Downward longwave / Upward longwave	246.1 [240.3] / −273.8 [−271.4]	246.2 [240.6] / −273.7 [−271.6]	260.1 [262.8] / −297.2 [−298.2]	260.5 [262.8] / −295.0 [−297.9]

ble 4) and the surface wind stress on Antarctic sea ice in the inner part of the exterior region from 70 to 180° E is weaker (Figs. 4, A5, Table 3).

3.2 Sea ice drift

3.2.1 Ice drift magnitude and its links with ice concentration, ice thickness and wind stress

The Arctic and Antarctic ice drift magnitude and direction simulations are improved from OMIP1 to OMIP2 (Lin et al., 2021). To understand the factors responsible for this feature, the sensitivity of the ice drift magnitude simulation to the changes in ice concentration, ice thickness and surface wind stress is investigated. The mean kinetic energy (MKE) is calculated to measure the ice drift magnitude,

$$\text{MKE} = \frac{1}{2}\left(u^2 + v^2\right),\tag{1}$$

where u and v are zonal and meridional components of ice drift, respectively. The simulated monthly mean and spatially averaged values of the ice MKE and their links with the ice concentration, ice thickness and surface wind stress are examined for NorESM2-LM (Arctic in Fig. 7 and Antarctic in Fig. 8) and CMCC-CM2-SR5 and MRI-ESM2-0 (Arctic in

Fig. A8 and Antarctic in Fig. A9). Spatial averages are computed for the interior and exterior regions with ice-free drift or not as defined in Sect. 3.1, based on the NSIDC-0051 ice concentration in each hemisphere and different months. As introduced in Lin et al. (2021), the ice vectors from observations and models are removed when ice concentrations are below 50 % or the data are closer than 75 km to the coast or have a spurious value. To be consistent, we apply these selections to other variables in the calculation.

In the Arctic interior region, the ice-motion MKE in NorESM2-LM/C (Fig. 7a, solid orange) is larger than those in KIMURA (solid blue) and ICDC-NSIDCv4.1 data (solid purple), and this positive bias is slightly reduced in NorESM2-LM/J (solid green) from January to April and September. The largest improvement in the interior ice-motion MKE occurs in September (Fig. 7b, solid black). It is mostly caused by the increased ice concentration and thickness in NorESM2-LM/J (Fig. 7c to f), while the changes in the surface wind stress are very small (Fig. 7g to h). The September ice concentration in NorESM2-LM/J is close to NSIDC-0051 and OSI-450 data (Fig. 7c). The observational Arctic ice thickness data in September are not available for comparison (Fig. 7e). The ice thickness observations during 2003–2007 are restricted to a few months per year in both
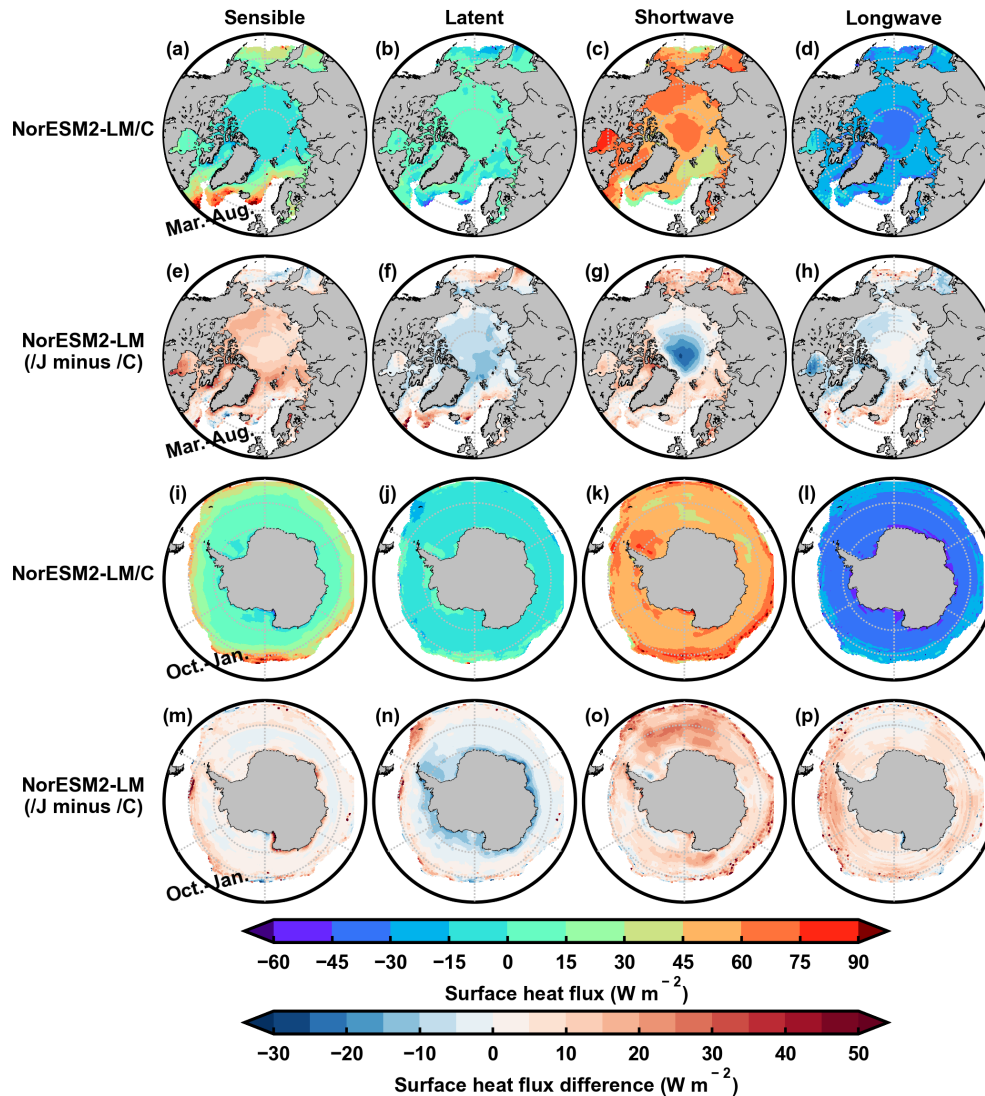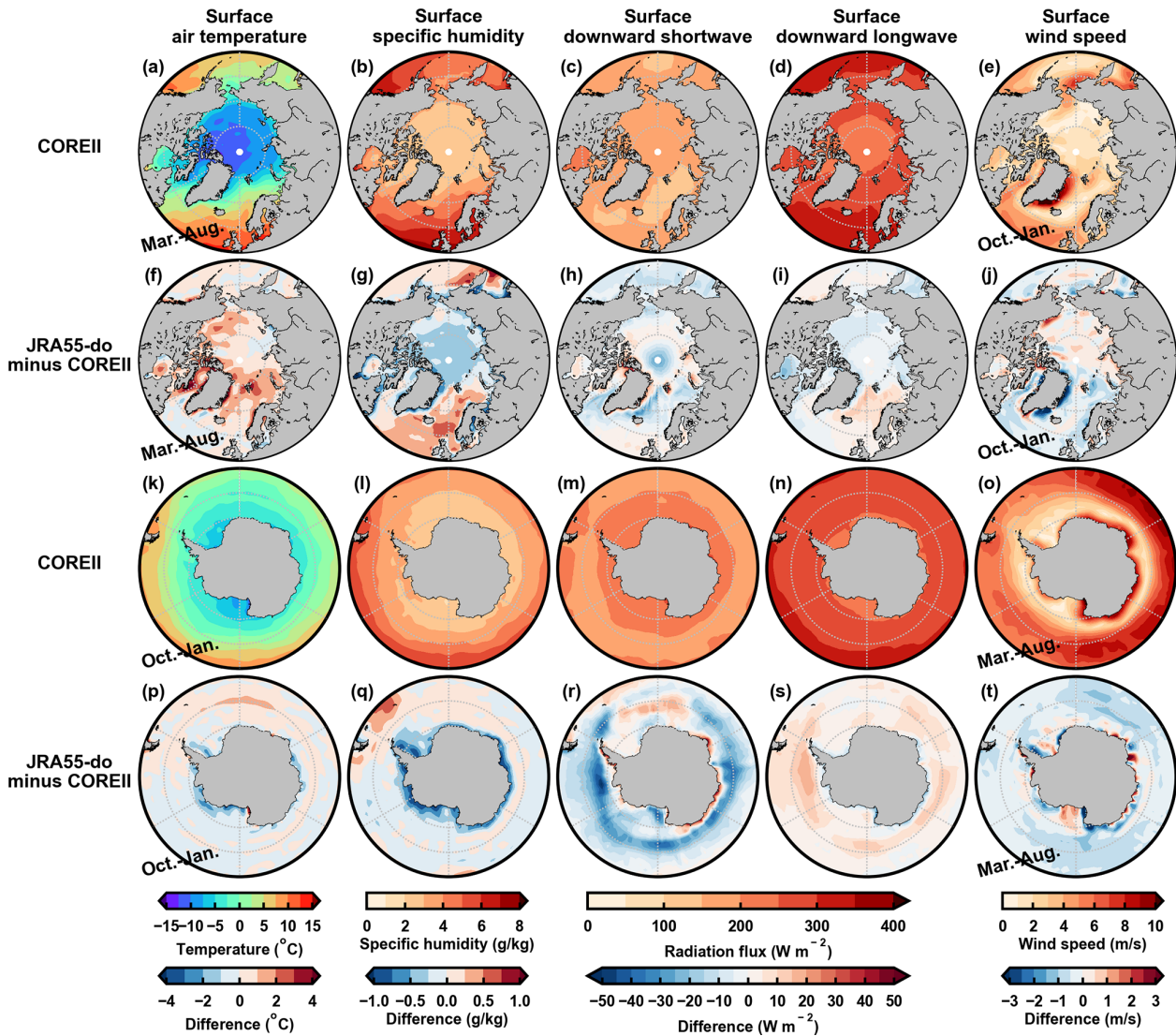
Figure 5. 1980–2007 March–August mean Arctic **(a–h)** and October–January mean Antarctic **(i–p)** surface sensible (first column) and latent (second column) heat fluxes and net shortwave (third column) and longwave (fourth column) radiation fluxes. The positive values indicate a surface flux downward. The first and third rows correspond to NorESM2-LM/C, and the second and fourth rows are differences between NorESM2-LM/J and NorESM2-LM/C.

the Envisat and ICESat datasets. The Envisat ice thickness data are provided from November to April for the Arctic with coverage up to 81.5° N and from May to October for the Antarctic. The measurement campaigns of ICESat ice thickness are for the months of February–March, March–April, May–June and October–November, with each campaign lasting roughly 33 d. The comparisons between individual models and the two observational references are thus restricted to these months when data are available (Figs. 7e and 8e). Compared to the OMIP1 simulation, the Arctic interior ice-motion MKE from January to December is not much improved in CMCC-CM2-SR5/J, MRI-ESM2-0/J, EC-Earth3/J and MIROC6/J (Fig. A8a to d). The positive September ice-motion MKE bias in NorESM2-LM/C is larger than in

other OMIP1 models, and this positive bias is reduced in NorESM2-LM/J but not in other models.

In the Arctic exterior region, the ice-motion MKE in the five OMIP1 simulations (Figs. 7a, A8a to d, dashed orange) is much larger than those in KIMURA (dashed blue) and ICDC-NSIDCv4.1 data (dashed purple), and the positive biases in OMIP1 simulations are largely reduced in OMIP2 simulations (dashed green) from November to April. The decreased Arctic ice-motion MKE in OMIP2 simulations in the exterior region from November to April is mainly induced by the decreased surface wind stress (Figs. 7g and h, A8m and n), while the changes in ice concentration and thickness are very small (Figs. 7c to f and A8e to l). There is no consistent improvement in the representation of sea ice concentra-

Figure 6. 1980–2007 March–August mean Arctic and October–January mean Antarctic surface air temperature (first column) and specific humidity (second column), downward shortwave (third column) and longwave radiation (fourth column) fluxes, and October–January mean Arctic and March–August mean Antarctic surface wind speeds (fifth column). The first and third rows correspond to CORE-II, and the second and fourth rows are differences between JRA55-do and CORE-II.

tion and thickness during November to April from OMIP1 to OMIP2 simulations. We average modeled ice thickness limited up to 81.5° N as in Envisat data, and this affects the ice thickness in the summer months but not from November to April. The sea ice thickness is larger in summer than in winter in models (Figs. 7e and A8i to l). As explained before, regions selected to do the spatial average are different in each month in our calculation, and this can affect the monthly mean ice thickness. When open water is included in calculating the spatial average of ice thickness, the summer maximum in ice thickness does not exist. The annual maximum and minimum in ice mass are in spring and late summer, respectively. Multi-category sea ice models assume that all sea ice categories melt at the same rate. Consequently, thin ice

melts away first, and thicker deformed ice remains until late summer. Then, mean ice thickness could be larger in summer than in winter, in particular when the total ice concentration is low.

In the Antarctic interior region, the ice-motion MKE in NorESM2-LM/C (Fig. 8a, solid orange) is larger than those in KIMURA (solid blue) and ICDC-NSIDCv4.1 data (solid purple), and this positive bias is reduced in April in NorESM2-LM/J (solid green, smaller than -1×10^{-3} m^2 s^{-2} as a baseline). The decreased Antarctic ice-motion MKE in the interior region in April (Fig. 7b, solid black) is consistent with the increased ice concentration and thickness but not the increased surface wind stress in NorESM2-LM/J (Fig. 7d, f and h, solid black). However, the ice concentration and thick-
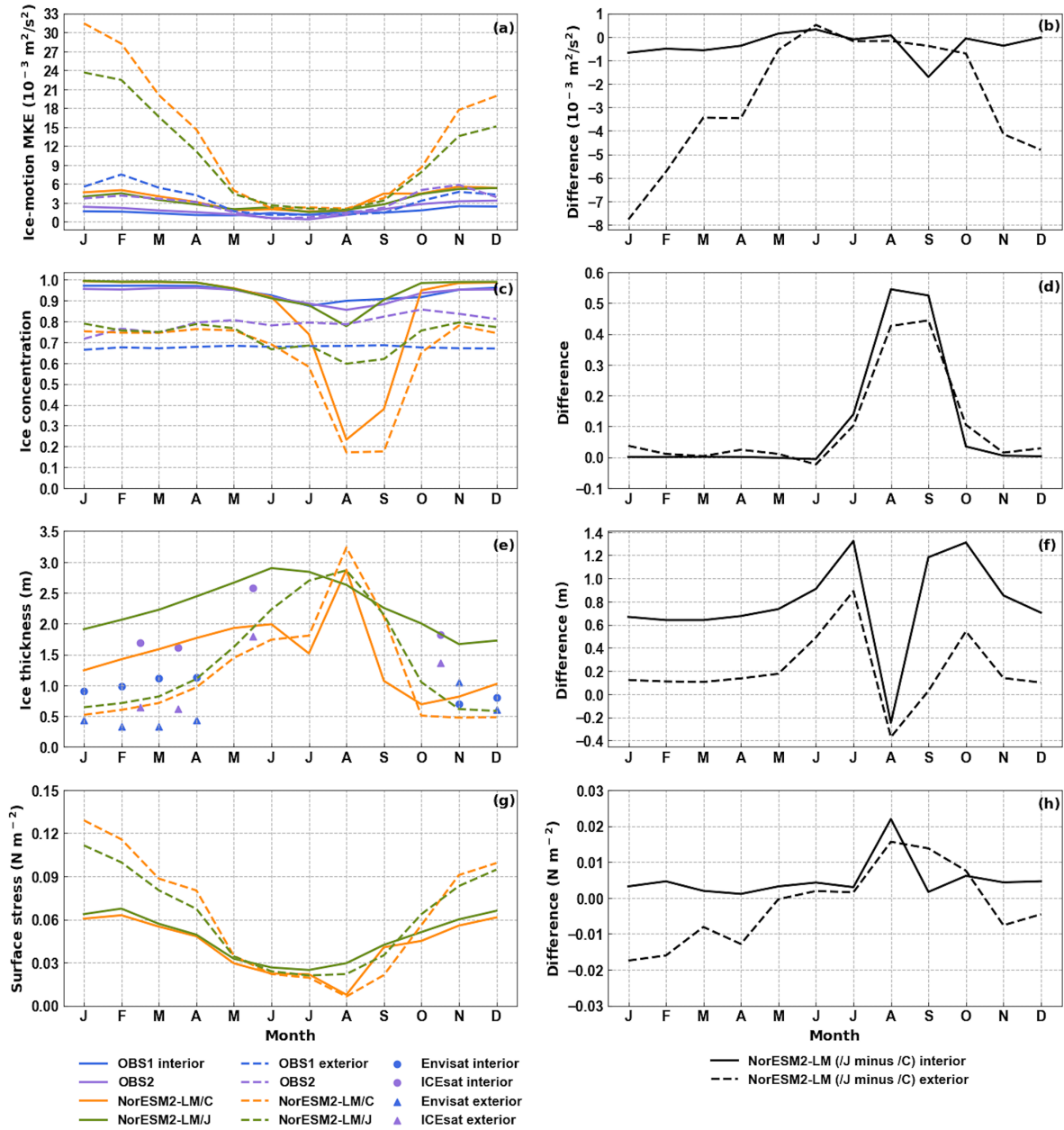
Figure 7. 2003–2007 monthly mean and spatially averaged Arctic ice kinetic energy (MKE) **(a)**, ice concentration **(c)**, ice thickness **(e)** and surface wind stress **(g)** from observations (blue and purple), NorESM2-LM/C (orange) and NorESM2-LM/J (green). Two observational datasets are included for ice-motion MKE (KIMURA and ICDC-NSIDCv4.1), concentration (NSIDC-0051 and OSI-450) and thickness (Envisat and ICESat). The solid and dashed lines are spatial averages on the regions with ice concentrations larger (interior) and smaller (exterior) than 80 % in NSIDC-0051, respectively. The differences between NorESM2-LM/J and NorESM2-LM/C ice-motion MKE **(b)**, ice concentration **(d)**, ice thickness **(f)** and surface wind stress **(h)** in the interior (solid black) and exterior (dashed black) regions are shown.

ness are also increased in NorESM2-LM/J from December to March, similarly to April, while the ice-motion MKE is not reduced. This suggests that the ice motion at the beginning of the melting season is not that sensitive to the ice concentration and thickness changes. Olason and Notz (2014) showed that the Arctic ice drift speed in April and May is not correlated with ice concentration or thickness, and the

increase in drift speed is due to newly formed fractures without changes in ice concentration. This indicates that the unreduced Antarctic ice-motion MKE from December to March in NorESM2-LM/J can be related to newly formed fractures even though the increases in ice concentration and thickness are similar to that in April. Compared to the OMIP1 simulation, the Antarctic interior ice-motion MKE from January
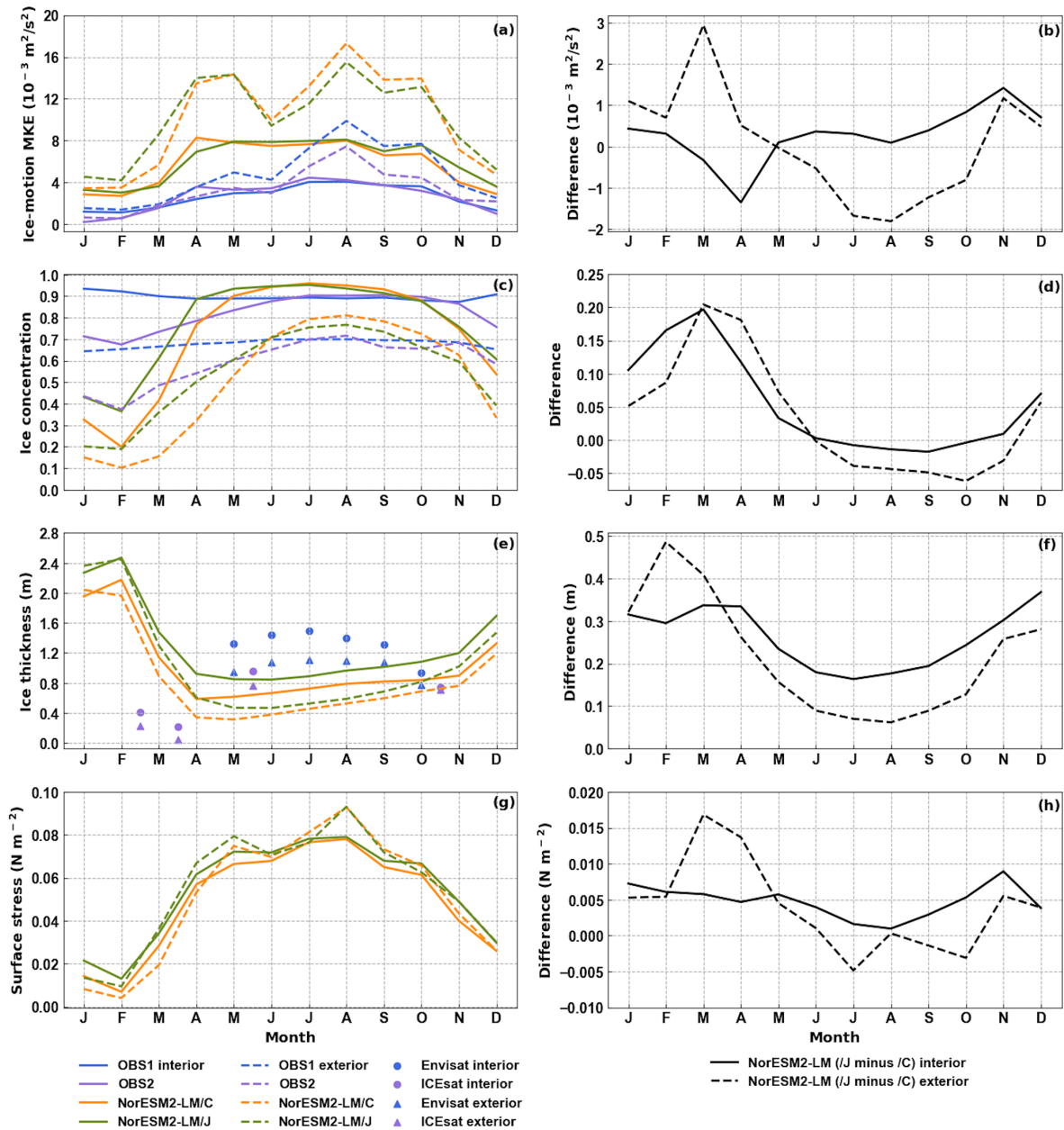
Figure 8. Same as Fig. 7 but for the Antarctic. The Envisat ice thickness data are provided from May to October.

to December is not much improved in CMCC-CM2-SR5/J, MRI-ESM2-0/J, EC-Earth3/J and MIROC6/J (Fig. A9a to d).

In the Antarctic exterior region, the ice-motion MKE in NorESM2-LM/C (Fig. 8a, dashed orange) is larger than those in KIMURA (dashed blue) and ICDC-NSIDCv4.1 data (dashed purple), and this positive bias is reduced in NorESM2-LM/J from July to September (dashed green, smaller than $-1 \times 10^{-3}\,\mathrm{m^2\,s^{-2}}$ as a baseline). The ice-motion MKE positive bias is reduced from July to October in CMCC-CM2-SR5/J, MRI-ESM2-0/J, EC-Earth3 and MIROC6 (Fig. A9a to d, dashed black). The reduced ice-motion MKE in NorESM2-LM/J, CMCC-CM2-SR5/J and

MRI-ESM2-0/J is related to the decreased wind stress and increased ice thickness (Figs. 8f and h, A9i, j, m and n, dashed black). The reduced positive bias of ice-motion MKE in the Antarctic exterior region is much smaller than those in the Arctic in OMIP2 simulations (Figs. 8b vs. 7b, A9a to d vs. A8a to d, dashed black).

3.2.2 Ice drift direction and its connections to wind stress

We finally aim at determining to what extent the change in atmospheric forcing may lead to an improvement in the sim-
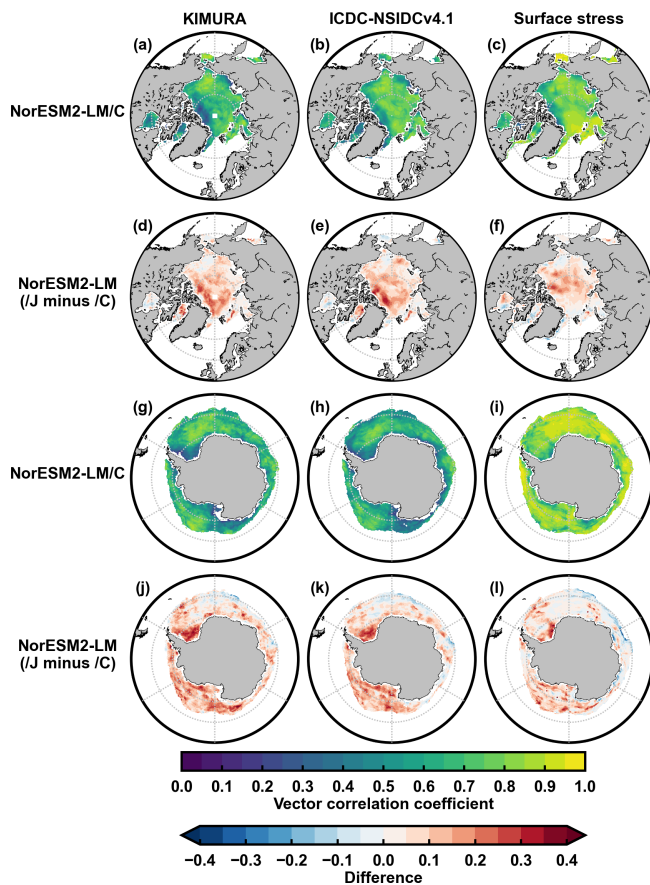
Figure 9. The significant vector correlation coefficients during 2003–2007 at a level of 99 % between modeled ice drift (NorESM2-LM/C) and two observational data (KIMURA and ICDC-NSIDCv4.1), respectively, and between NorESM2-LM/C-modeled ice drift and surface wind stress in the Arctic **(a–c)** and Antarctic **(g–i)**. The second and fourth rows are the vector correlation coefficient differences by changing the modeled ice drift from NorESM2-LM/C to NorESM2-LM/J.

ulated ice drift direction (independently of the improvements in sea ice drift magnitude noted in the previous section). To that end, the vector correlations between simulated and observed ice drift fields (KIMURA and ICDC-NSIDCv4.1 data) are diagnosed, as done in Lin et al. (2021). In general, the vector correlation coefficients between the modeled ice drift and observational data during 2003–2007 are larger in NorESM2-LM/J than those in NorESM2-LM/C in the Arctic (Fig. 9d and e) and Antarctic (Fig. 9j and k).

The links with the surface wind stress are assessed. The vector correlation coefficients between modeled ice drift and surface wind stress are much larger in NorESM2-LM/J than those in NorESM2-LM/C in the Beaufort Gyre area (Fig. 9f) and the Pacific and Atlantic sectors of the Southern Ocean (Fig. 9l). Those regions correspond to large improvements in the ice vector direction simulation in NorESM2-LM/J (Fig. 9d, e, j and k). This suggests that the improved ice

vector direction simulation is related to the changed surface wind stress in NorESM2-LM/J. These improvements can also be found in CMCC-CM2-SR5/J, MRI-ESM2-0/J, EC-Earth3/J and MIROC6/J in both hemispheres (Fig. A10), but the improvements in MRI-ESM2-0/J, EC-Earth3/J and MIROC6/J are smaller than those in NorESM2-LM/J and CMCC-CM2-SR5/J in the Arctic.

4 Conclusions and discussion

OMIP provides useful datasets for reconstructing sea ice evolution over the past decades. Lin et al. (2021) have shown that the accuracy of the reconstruction depends on the atmospheric forcing used. This paper attempts to explain why this is so by conducting surface momentum and heat flux analyses. The two atmospheric reanalysis products are different in both dynamical and thermodynamical components for the Arctic and Antarctic, such as the air temperature and winds, which contribute to heat flux and momentum flux differences in the ocean–sea ice models. We studied the dynamic and thermodynamic processes contributing to the ice concentration tendencies and their links with surface heat and momentum fluxes as well as the connections between the simulated ice drift and the ice concentration, ice thickness and wind stress.

In general, the sea ice concentration and ice drift magnitude and direction simulations are improved from OMIP1 to OMIP2, and improvements in the Arctic are larger than those in the Antarctic. The net surface heat fluxes are decreased in the interior region, with ice concentration above 80 %, and increased in the CAA and CWS regions during March to August (Arctic) and October to January (Antarctic) in OMIP2 compared to OMIP1 simulations. This can explain the improved OMIP2 ice concentration simulations in the summer, pointing to the important role played by the thermodynamic processes during the ice-melting season. The changed net shortwave radiation fluxes from OMIP1 to OMIP2 simulations are crucial for improving the OMIP2 summer ice concentration simulations in the Arctic interior, CAA and CWS regions. The decreased surface wind stress in the inner part of the exterior region during March to August in OMIP2 compared to OMIP1 contributes to the improved (decreased) Antarctic September OMIP2 ice concentration simulation in the exterior region from 70 to 180° E, pointing to the dominant role of dynamic processes. The monthly mean and spatially averaged Arctic ice-motion MKE simulation in the exterior region is improved (decreased) from November to April due to the decreased surface wind stress in OMIP2 compared to OMIP1 simulations, while the improvement in the Antarctic is small. The improved surface wind stress simulation in the Beaufort Gyre area and the Pacific and Atlantic sectors of the Southern Ocean can help improve the ice vector direction simulation.

This study provides clues to improve the atmospheric reanalysis products for a better sea ice simulation in ocean–sea ice models. The net shortwave radiation fluxes during the ice-melting season in the interior region and the wind stress during the ice-expansion season in the exterior region are crucial for a better sea ice concentration simulation. The wind stress is also important to the sea ice drift magnitude and vector direction simulations. Some aspects of the sea ice simulation are not improved by changing the forcing from CORE-II to JRA55-do, such as the winter Arctic ice concentration in the exterior region, summer Antarctic ice concentration in the coastal regions and ice drift magnitude in some months. The biases in surface heat fluxes and surface stress in these regions and periods are large compared to ERA5 reanalysis data (not shown). Improving Antarctic radiation fluxes and Arctic and Antarctic winds in the atmospheric reanalysis products can be helpful for reducing the bias. The limited impact of atmospheric forcing on ice concentration simulation was discussed in Barthélemy et al. (2018). In these exterior and coastal regions, thermodynamic processes tend to compensate for the changes caused by dynamic processes, and properly combined contributions from thermodynamic and dynamic processes are needed to improve the simulations. Both atmospheric forcing and model physics of the sea ice growth and melt processes are crucial for an improved simulation in these aspects. Differences are shown in OMIP models with different sea ice models. For example, the summer sea ice concentration conditions in NorESM2-LM (Fig. 1) and EC-Earth3 (Fig. A2) are different, which can be related to the different radiative schemes in CICE5.1.2 and LIM3 sea ice models as detailed in Table 1. The collaborations with model development groups are needed to help advance the sea ice simulation. We recommend that, in such intercomparison exercises, all the specificities/namelists of the sea ice models used should systematically be reported to help understand the different responses to model physics.

From our analysis, the differences in the atmospheric forcing are transferred to the modeled surface fluxes and contribute to the improved ice concentration simulation. However, tuning is also a key aspect in climate models that can explain differences in performance. It is possible that some groups could have tuned for OMIP2 and then used the same setup for OMIP1, so part of the improvement with OMIP2 could be due to this experimental setup choice. While this paper reiterates the importance of the atmospheric forcing for the representation of the sea ice state, it is expected, based on the conclusions, that errors in the atmospheric forcing will also affect the ocean through modified heat, freshwater and momentum fluxes between the ice and the ocean. These errors can thus eventually affect the representation of ocean temperature, salinity and currents.

Appendix A

In this Appendix, extra sea ice diagnostics from CMCC-CM2-SR5, MRI-ESM2-0, EC-Earth3 and MIROC6 are given to help support the conclusions derived from NorESM2-LM. The ice concentration simulations from four models are provided in Figs. A1 and A2. The effects of the thermodynamic and dynamic components of the atmospheric forcing in CMCC-CM2-SR5 and MRI-ESM2-0 are presented in Figs. A3 to A6. The surface heat flux on sea ice is not provided for MRI-ESM2-0, and the corresponding figures are not included in Figs. A5 and A6. The downward and upward shortwave radiation fluxes in NorESM2-LM and CMCC-CM2-SR5 are added in Fig. A7. The ice drift simulation and the relationship with ice concentration, ice thickness and wind stress in CMCC-CM2-SR5, MRI-ESM2-0, EC-Earth3 and MIROC6 are provided in Figs. A8 to A10.
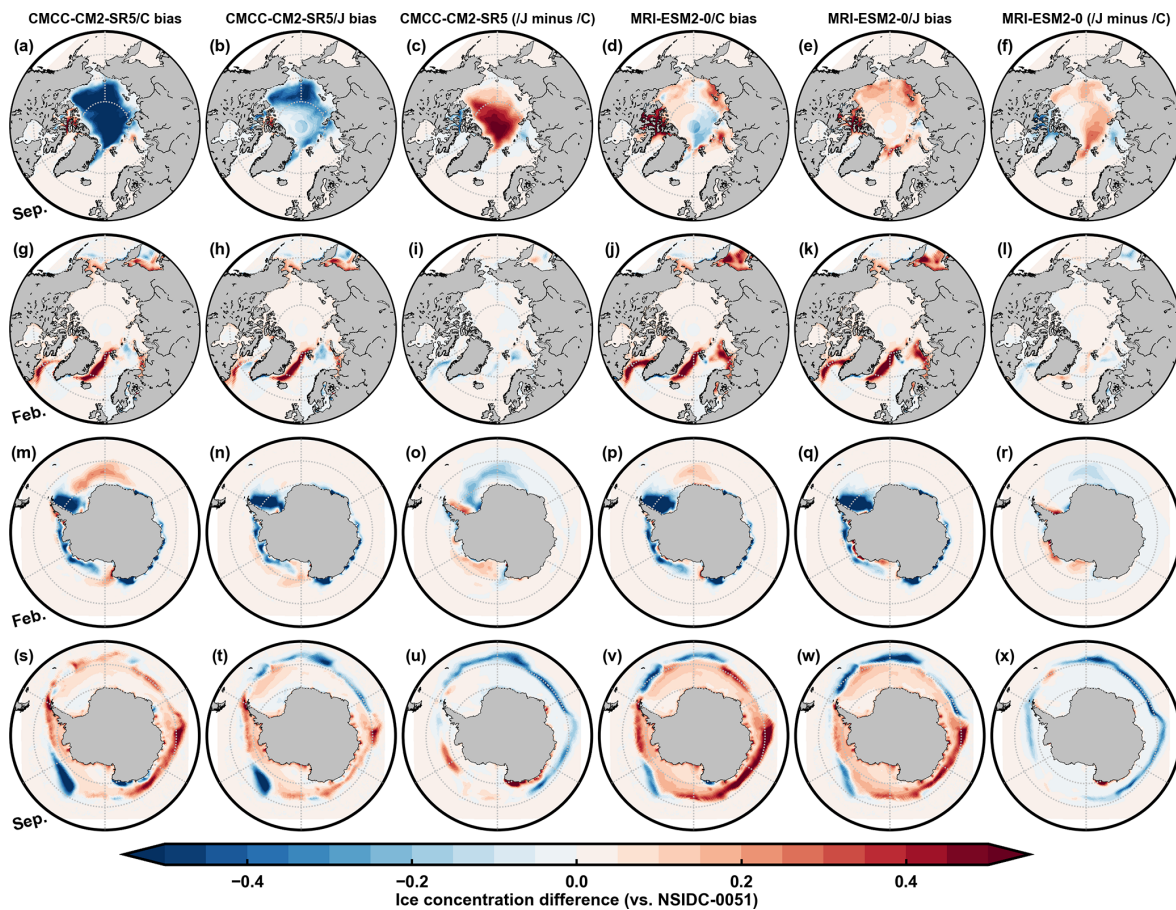
Figure A1. 1980–2007 September and February mean Arctic **(a–l)** and Antarctic **(m–x)** sea ice concentration differences between CMCC-CM2-SR5/C and NSIDC-0051 (first column), CMCC-CM2-SR5/J and NSIDC-0051 (second column), CMCC-CM2-SR5/J and CMCC-CM2-SR5/C (third column), MRI-ESM2-0/C and NSIDC-0051 (fourth column), MRI-ESM2-0/J and NSIDC-0051 (fifth column), and MRI-ESM2-0/J and MRI-ESM2-0/C (sixth column).
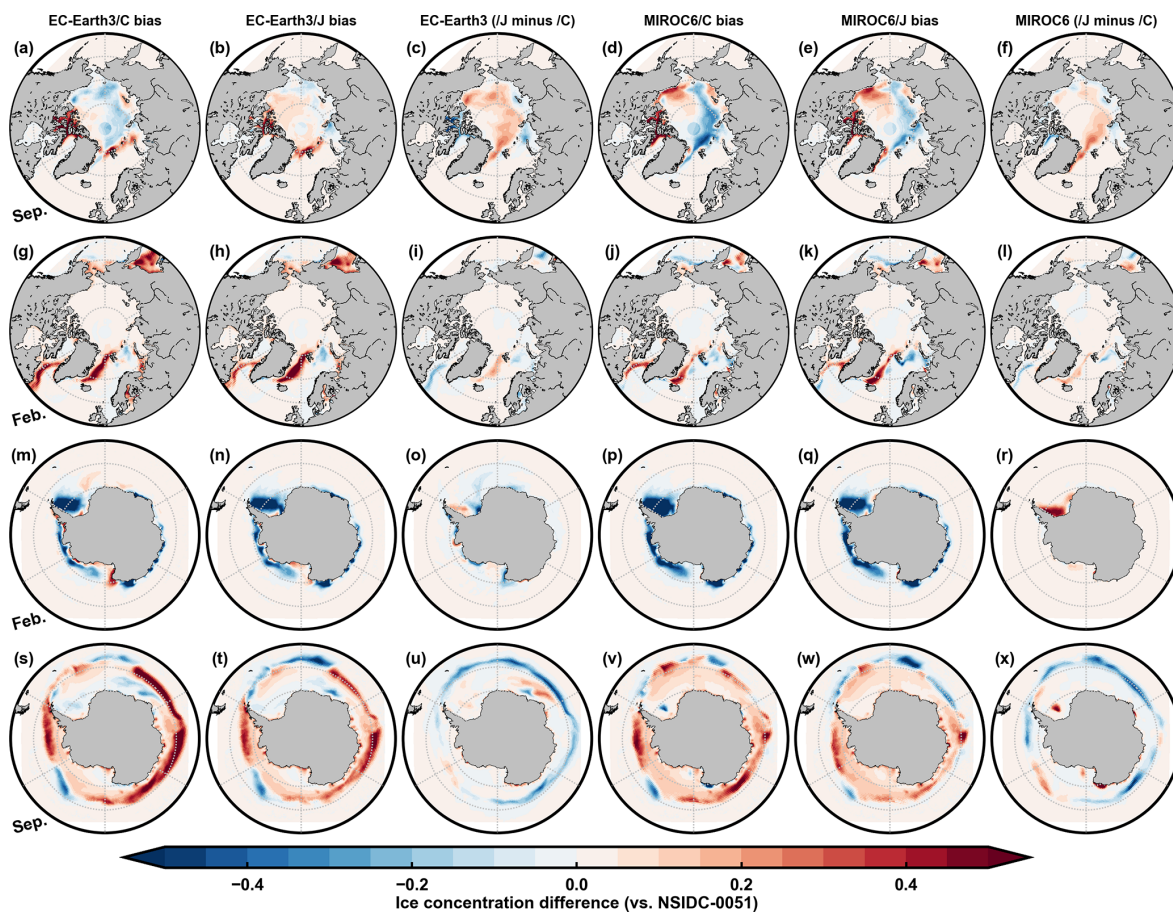
Figure A2. 1980–2007 September and February mean Arctic **(a–l)** and Antarctic **(m–x)** sea ice concentration differences between EC-Earth3/C and NSIDC-0051 (first column), EC-Earth3/J and NSIDC-0051 (second column), EC-Earth3/J and EC-Earth3/C (third column), MIROC6/C and NSIDC-0051 (fourth column), MIROC6/J and NSIDC-0051 (fifth column) and MIROC6/J and MIROC6/C (sixth column).
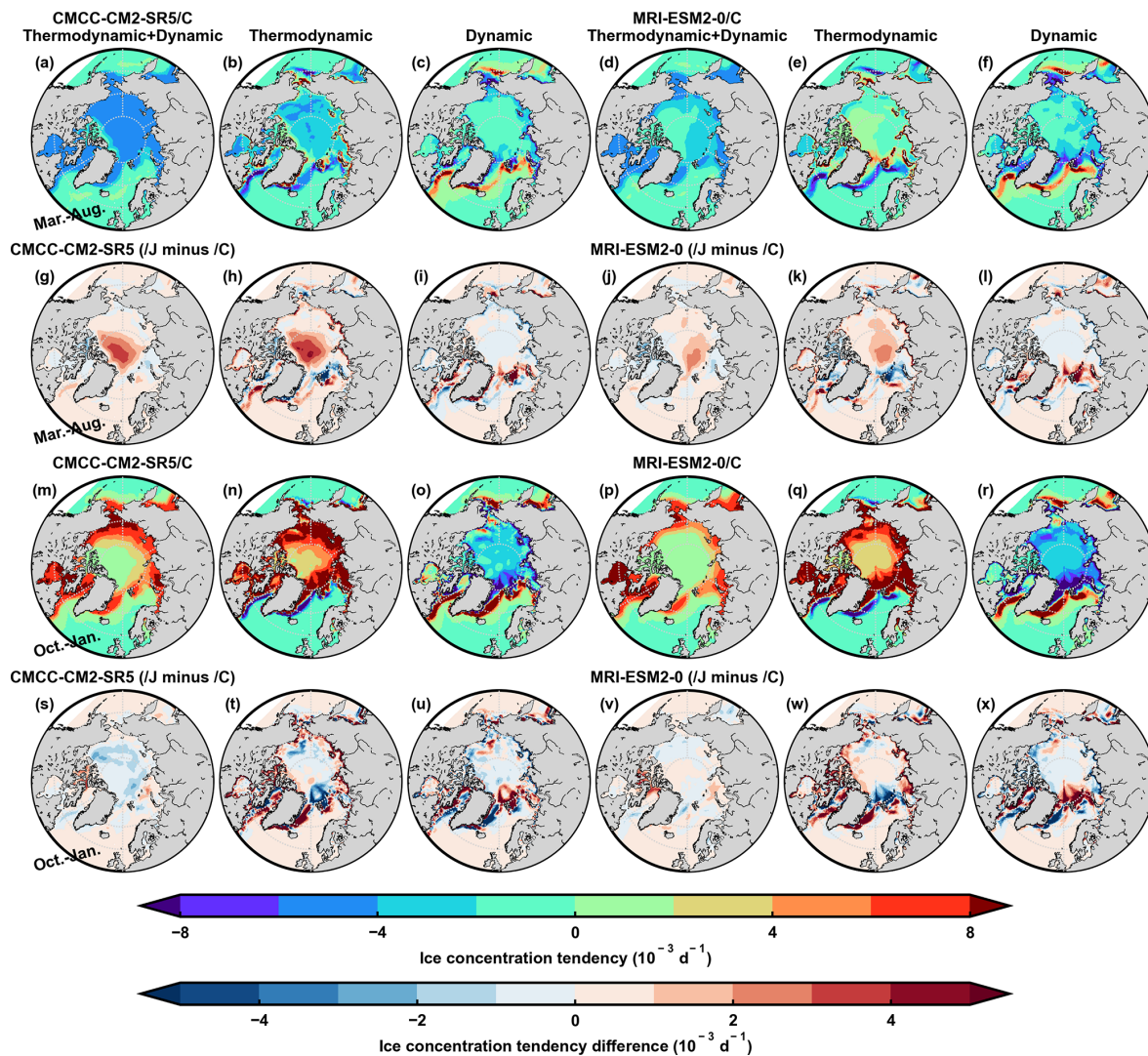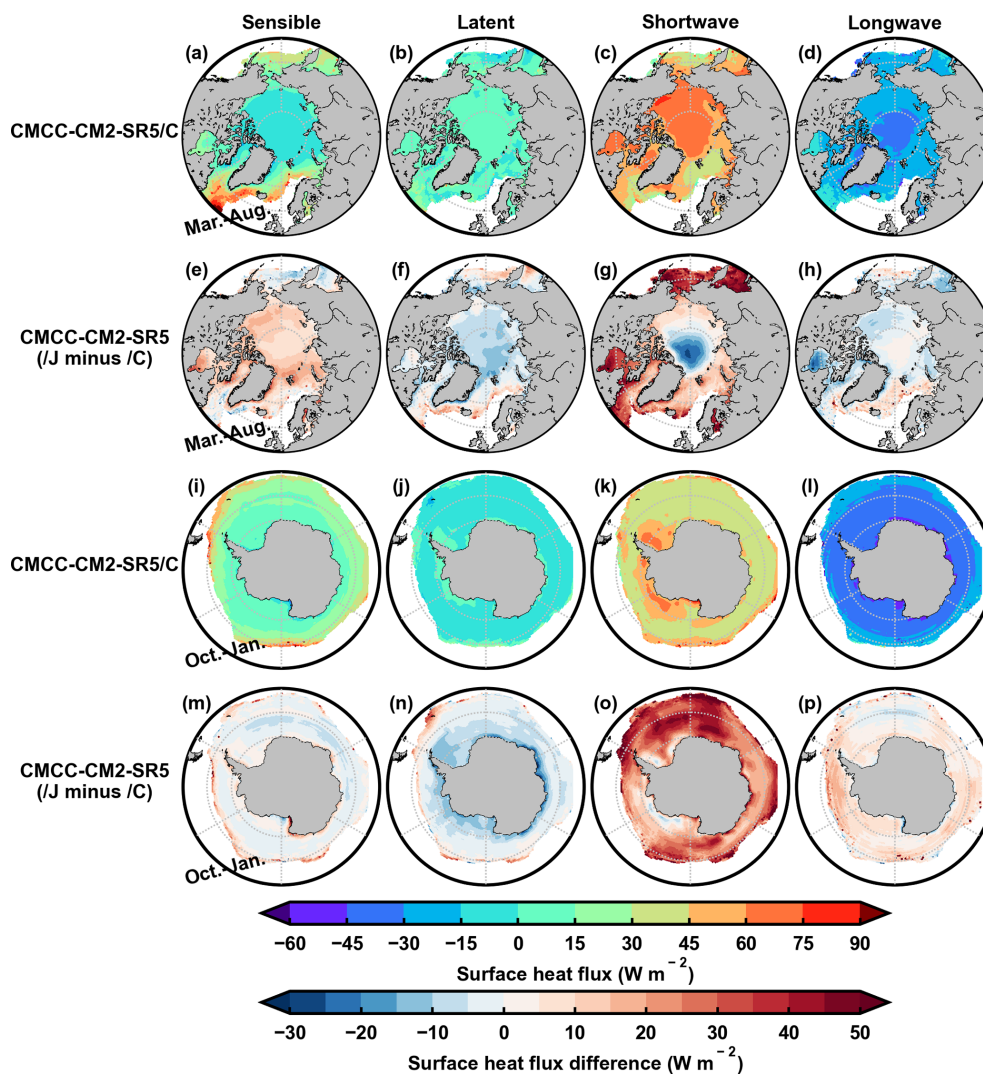
Figure A3. 1980–2007 March–August **(a–l)** and October–January **(m–x)** mean Arctic sea ice concentration tendencies in CMCC-CM2-SR5 (first three columns) and MRI-ESM2-0 (last three columns) due to thermodynamic and dynamic processes in total (first and fourth columns), thermodynamic processes (second and fifth columns) and dynamic processes (third and sixth columns). The first and third rows are from CMCC-CM2-SR5/C and MRI-ESM2-0/C, and the second and fourth rows are differences between CMCC-CM2-SR5/J and CMCC-CM2-SR5/C and between MRI-ESM2-0/J and MRI-ESM2-0/C, respectively.
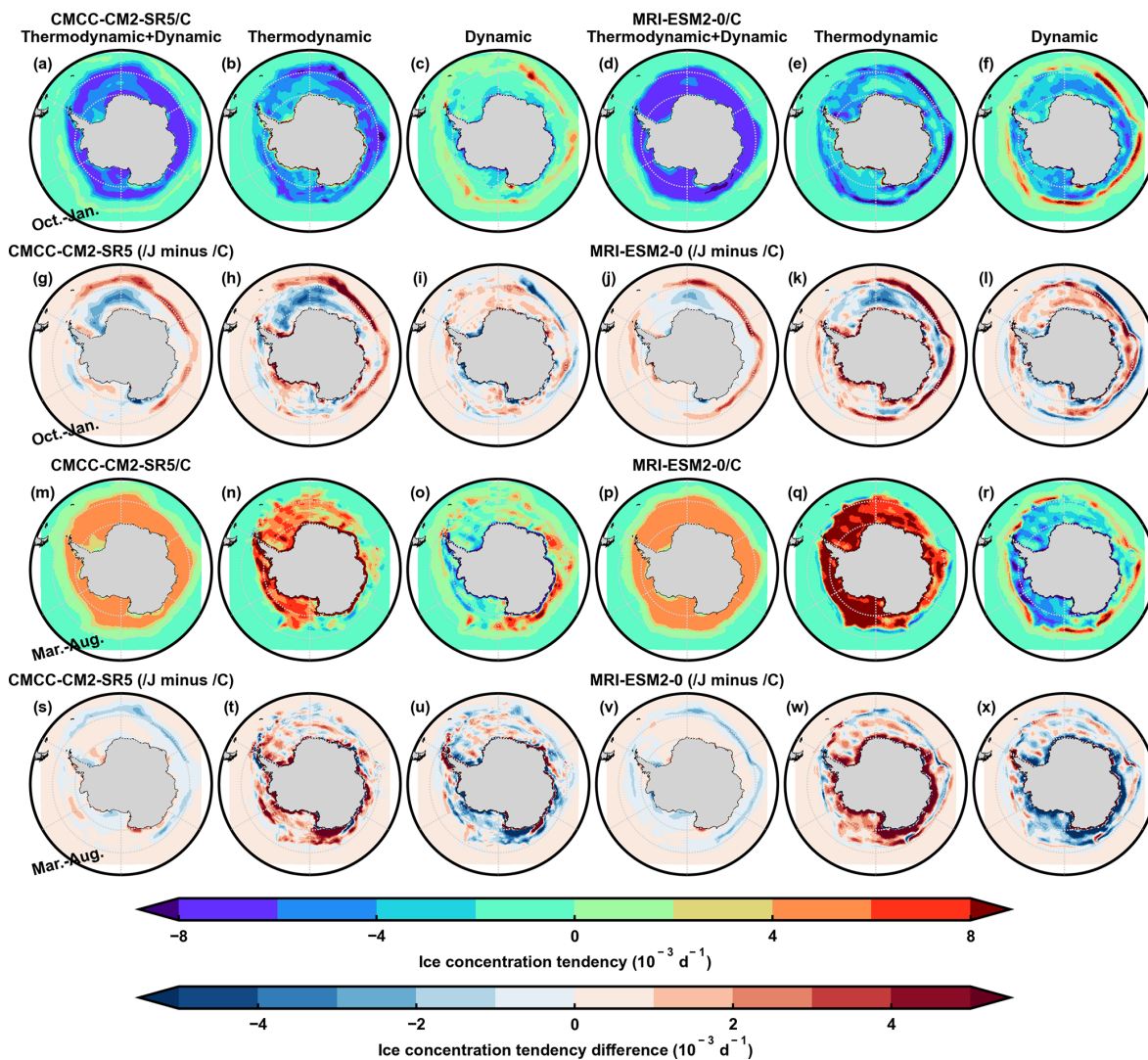
Figure A4. Same as Fig. A3 but for the 1980–2007 October–January **(a–l)** and March–August **(m–x)** mean Antarctic sea ice concentration tendencies.
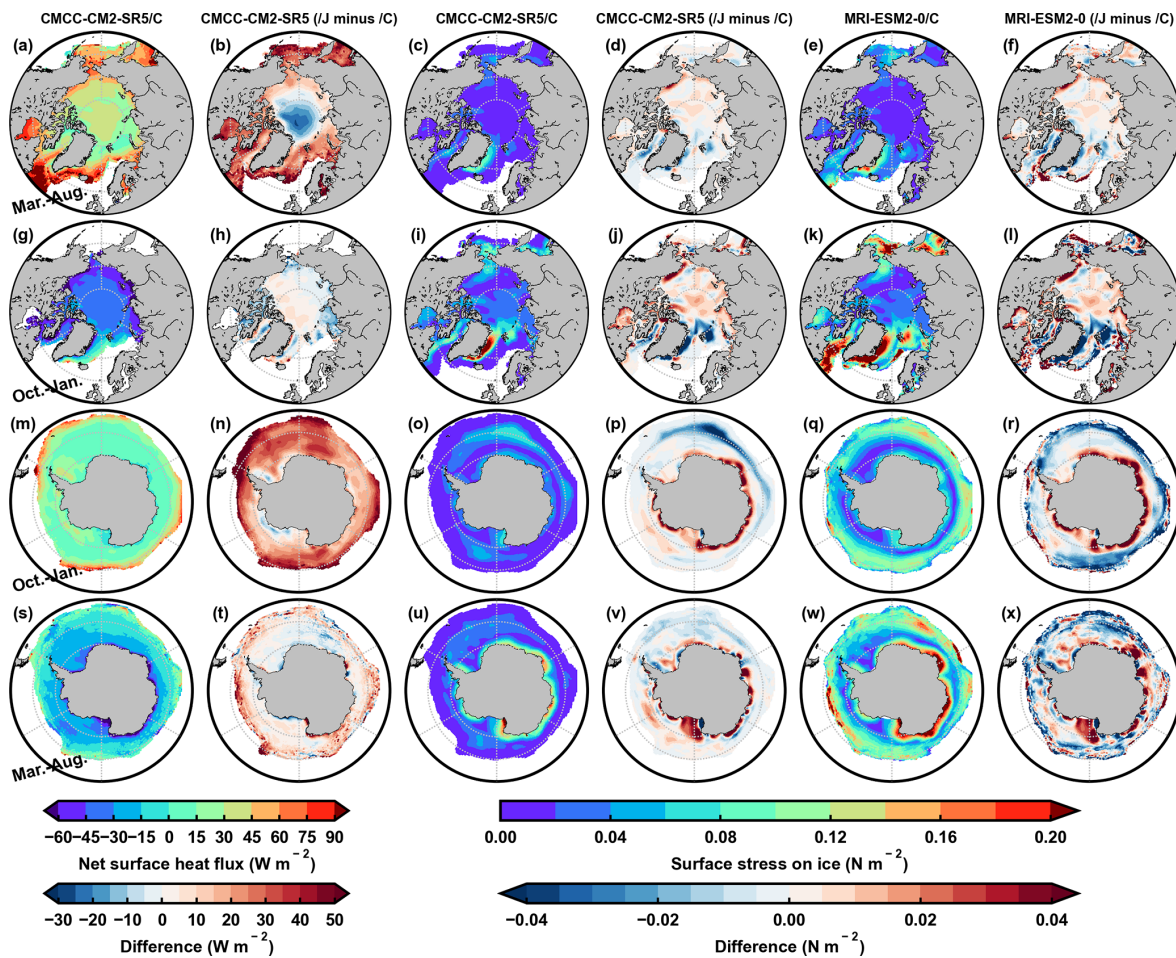
Figure A5. 1980–2007 March–August and October–January mean Arctic **(a–l)** and Antarctic **(m–x)** net surface heat flux (first two columns) and surface stress (last four columns) on sea ice. The positive values indicate a surface flux downward. The first and third columns correspond to CMCC-CM2-SR5/C, and the second and fourth columns are differences between CMCC-CM2-SR5/J and CMCC-CM2-SR5/C. The fifth column corresponds to MRI-ESM2-0/C, and the sixth column is the difference between MRI-ESM2-0/J and MRI-ESM2-0/C.

Figure A6. 1980–2007 March–August mean Arctic **(a–h)** and October–January mean Antarctic **(i–p)** surface sensible (first column) and latent heat fluxes (second column) and net shortwave (third column) and longwave (fourth column) radiation fluxes. The positive values indicate a surface flux downward. The first and third rows correspond to CMCC-CM2-SR5/C, and the second and fourth rows are differences between CMCC-CM2-SR5/J and CMCC-CM2-SR5/C.
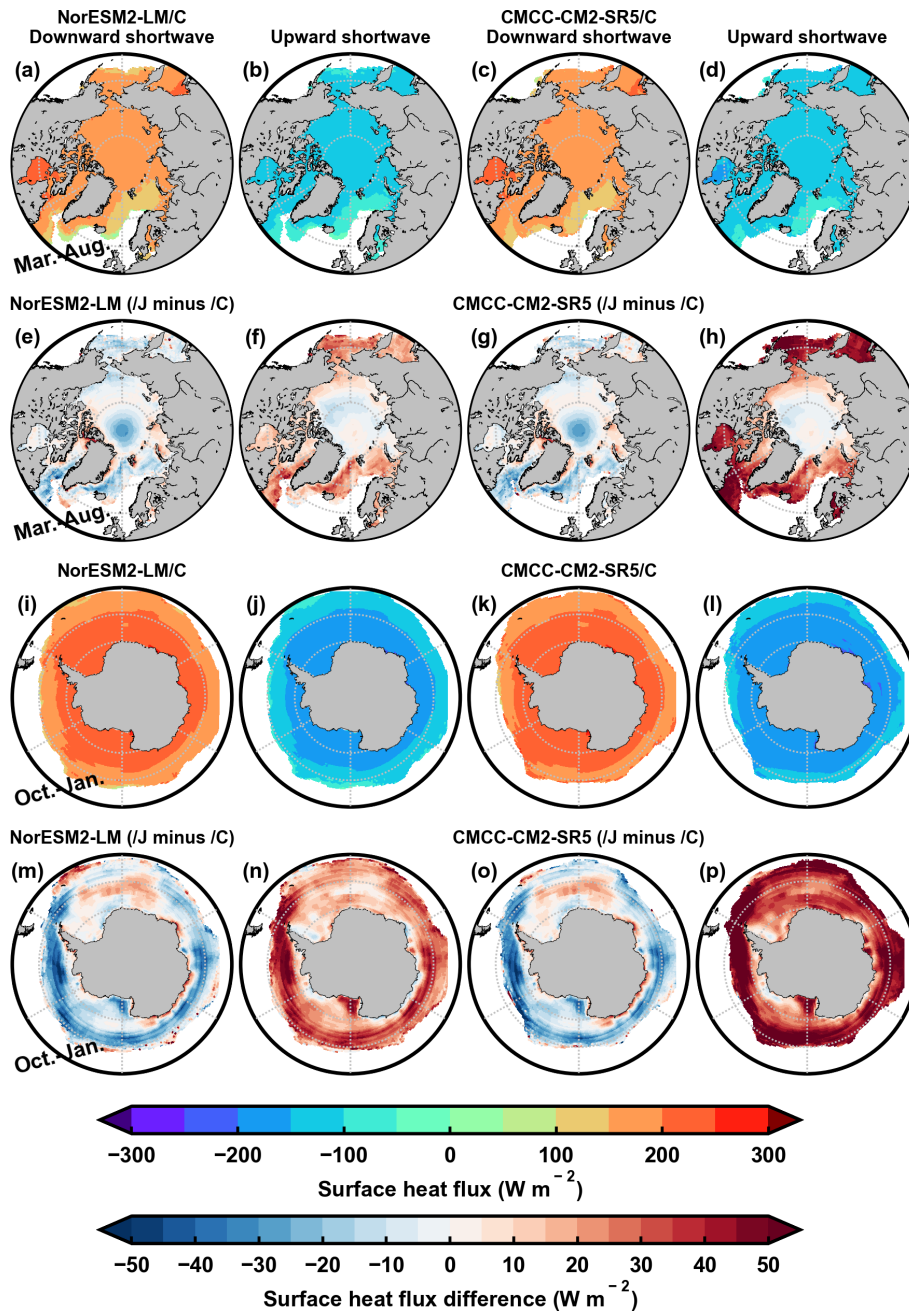
Figure A7. 1980–2007 March–August mean Arctic **(a–h)** and October–January mean Antarctic **(i–p)** downward and upward shortwave radiation fluxes in NorESM2-LM (first two columns) and CMCC-CM2-SR5 (last two columns). The positive values indicate a surface flux downward. The first and third rows correspond to model/C, and the second and fourth rows are differences between model/J and model/C.
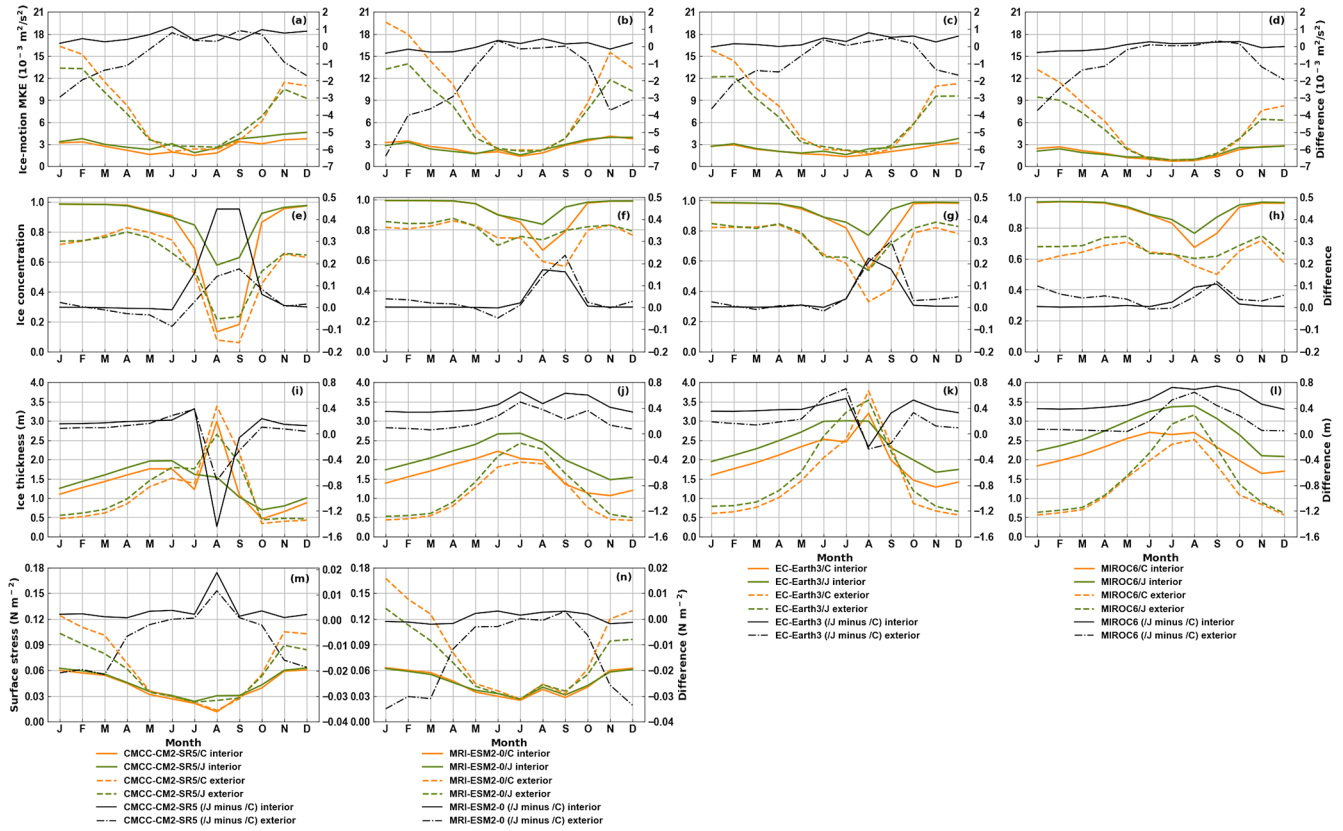
Figure A8. 2003–2007 monthly mean and spatially averaged Arctic ice kinetic energy (MKE) **(a–d)**, ice concentration **(e–h)**, ice thickness **(i–l)** and surface wind stress **(m–n)** in model/C (orange), model/J (green) and differences between model/J and model/C (black). The first to fourth columns correspond to CMCC-CM2-SR5, MRI-ESM2-0, EC-Earth3 and MIROC6 model results, respectively. The solid and dashed lines are spatial averages in the regions with ice concentrations larger (interior) and smaller (exterior) than 80 % in NSIDC-0051, respectively.
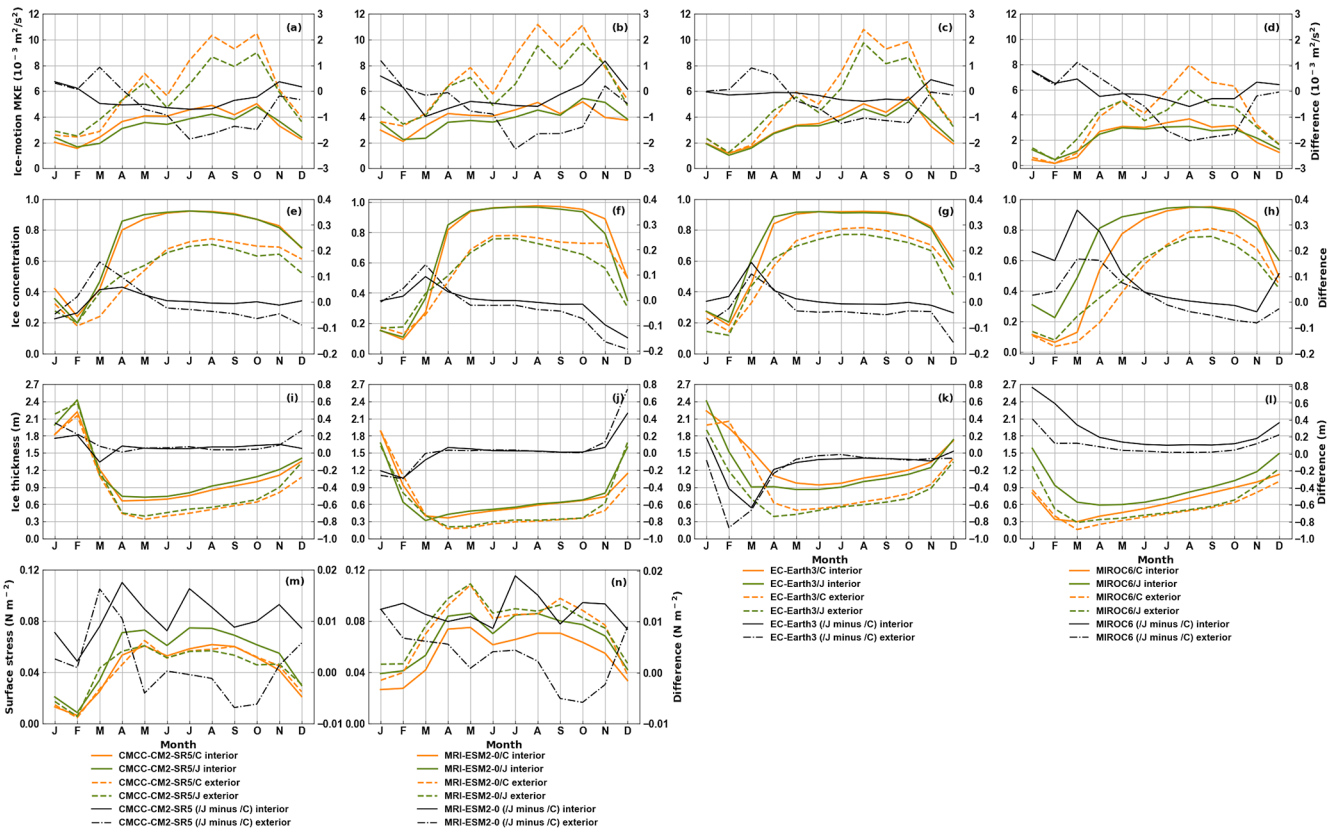
Figure A9. Same as Fig. A8 but for the Antarctic.
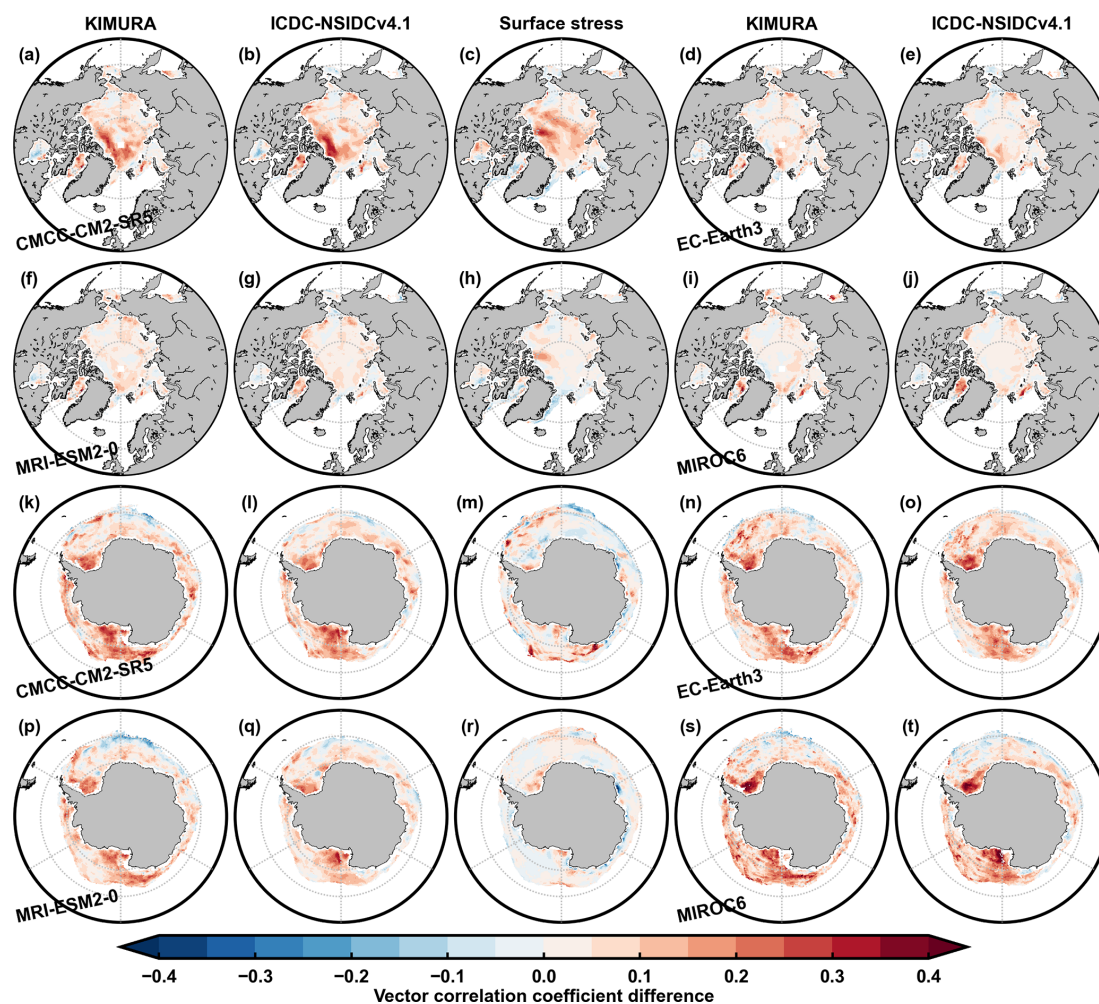
Figure A10. Differences in significant vector correlation coefficients during 2003–2007 at a level of 99 % between model/J and model/C in the Arctic **(a–j)** and Antarctic **(k–t)**. The first, second, fourth and fifth columns are significant vector correlation coefficients between modeled ice drift and KIMURA/ICDC-NSIDCv4.1 data, and the third column shows significant vector correlation coefficients between modeled (CMCC-CM2-SR5 and MRI-ESM2-0) ice drift and surface stress.

Review statement. This paper was edited by Jari Haapala and reviewed by two anonymous referees.

References

Barthélemy, A., Goosse, H., Fichefet, T., and Lecomte, O.: On the sensitivity of Antarctic sea ice model biases to atmospheric forcing uncertainties, Clim. Dynam., 51, 1585–1603, https://doi.org/10.1007/s00382-017-3972-7, 2018.

Bromwich, D. H., Wilson, A. B., Bai, L. S., Moore, G. W. K., and Bauer, P.: A comparison of the regional Arctic System Reanalysis and the global ERA-Interim Reanalysis for the Arctic, Q. J. Roy. Meteor. Soc., 142, 644–658, https://doi.org/10.1002/qj.2527, 2016.

Cavalieri, D. J., Parkinson, C. L., Gloersen, P., and Zwally, H. J.: Sea Ice Concentrations from Nimbus-7 SMMR and DMSP SSM/I-SSMIS Passive Microwave Data, Version 1, [1980–2007], Boulder, Colorado USA, NASA National Snow and Ice Data Center Distributed Active Archive Center [data set], https://doi.org/10.5067/8GQ8LZQVL0VL, 1996.

Chaudhuri, A. H., Ponte, R. M., and Forget, G.: Impact of uncertainties in atmospheric boundary conditions on ocean model solutions, Ocean Model., 100, 96–108, https://doi.org/10.1016/j.ocemod.2016.02.003, 2016.

Cherchi, A., Fogli, P. G., Lovato, T., Peano, D., Iovino, D., Gualdi, S., Masina, S., Scoccimarro, E., Materia, S., Bellucci, A., and Navarra, A.: Global Mean Climate and Main Patterns of Variability in the CMCC-CM2 Coupled Model, J. Adv. Model. Earth Sy., 11, 185–209, https://doi.org/10.1029/2018MS001369, 2019.

Chevallier, M., Smith, G. C., Dupont, F., Lemieux, J. F., Forget, G., Fujii, Y., Hernandez, F., Msadek, R., Peterson, K. A., Storto, A., Toyoda, T., Valdivieso, M., Vernieres, G., Zuo, H., Balmaseda, M., Chang, Y. S., Ferry, N., Garric, G., Haines, K., Keeley, S., Kovach, R. M., Kuragano, T., Masina, S., Tang, Y., Tsujino, H., and Wang, X.: Intercomparison of the arctic sea ice cover in global ocean–sea ice reanalyses from the ORA-IP project, Clim. Dynam., 49, 1107–1136, https://doi.org/10.1007/s00382-016-2985-y, 2017.

Comiso, J. C., Parkinson, C. L., Gersten, R., and Stock, L.: Accelerated decline in the Arctic sea ice cover, Geophys. Res. Lett., 35, 1–6, https://doi.org/10.1029/2007GL031972, 2008.

Ding, Q., Schweiger, A., L'Heureux, M., Battisti, D. S., Po-Chedley, S., Johnson, N. C., Blanchard-Wrigglesworth, E., Harnos, K., Zhang, Q., Eastman, R., and Steig, E. J.: Influence of high-latitude atmospheric circulation changes on summertime Arctic sea ice, Nat. Clim. Change, 7, 289–295, https://doi.org/10.1038/NCLIMATE3241, 2017.

Docquier, D., Massonnet, F., Barthélemy, A., Tandon, N. F., Lecomte, O., and Fichefet, T.: Relationships between Arctic sea ice drift and strength modelled by NEMO-LIM3.6, The Cryosphere, 11, 2829–2846, https://doi.org/10.5194/tc-11-2829-2017, 2017.

Döscher, R., Acosta, M., Alessandri, A., Anthoni, P., Arsouze, T., Bergman, T., Bernardello, R., Boussetta, S., Caron, L.-P., Carver, G., Castrillo, M., Catalano, F., Cvijanovic, I., Davini, P., Dekker, E., Doblas-Reyes, F. J., Docquier, D., Echevarria, P., Fladrich, U., Fuentes-Franco, R., Gröger, M., v. Hardenberg, J., Hieronymus, J., Karami, M. P., Keskinen, J.-P., Koenigk, T., Makkonen, R., Massonnet, F., Ménégoz, M., Miller, P. A., Moreno-Chamarro, E., Nieradzik, L., van Noije, T., Nolan, P., O'Donnell, D., Ollinaho, P., van den Oord, G., Ortega, P., Prims, O. T., Ramos, A., Reerink, T., Rousset, C., Ruprich-Robert, Y., Le Sager, P., Schmith, T., Schrödner, R., Serva, F., Sicardi, V., Sloth Madsen, M., Smith, B., Tian, T., Tourigny, E., Uotila, P., Vancoppenolle, M., Wang, S., Wårlind, D., Willén, U., Wyser, K., Yang, S., Yepes-Arbós, X., and Zhang, Q.: The EC-Earth3 Earth system model for the Coupled Model Intercomparison Project 6, Geosci. Model Dev., 15, 2973–3020, https://doi.org/10.5194/gmd-15-2973-2022, 2022.

Eyring, V., Bock, L., Lauer, A., Righi, M., Schlund, M., Andela, B., Arnone, E., Bellprat, O., Brötz, B., Caron, L.-P., Carvalhais, N., Cionni, I., Cortesi, N., Crezee, B., Davin, E. L., Davini, P., Debeire, K., de Mora, L., Deser, C., Docquier, D., Earnshaw, P., Ehbrecht, C., Gier, B. K., Gonzalez-Reviriego, N., Goodman, P., Hagemann, S., Hardiman, S., Hassler, B., Hunter, A., Kadow, C., Kindermann, S., Koirala, S., Koldunov, N., Lejeune, Q., Lembo, V., Lovato, T., Lucarini, V., Massonnet, F., Müller, B., Pandde, A., Pérez-Zanón, N., Phillips, A., Predoi, V., Russell, J., Sellar, A., Serva, F., Stacke, T., Swaminathan, R., Torralba, V., Vegas-Regidor, J., von Hardenberg, J., Weigel, K., and Zimmermann, K.: Earth System Model Evaluation Tool (ESMValTool) v2.0 – an extended set of large-scale diagnostics for quasi-operational and comprehensive evaluation of Earth system models in CMIP, Geosci. Model Dev., 13, 3383–3438, https://doi.org/10.5194/gmd-13-3383-2020, 2020.

Fogt, R. L., Sleinkofer, A. M., Raphael, M. N., and Handcock, M. S.: A regime shift in seasonal total Antarctic sea ice extent in the twentieth century, Nat. Clim. Change, 12, 54–62, https://doi.org/10.1038/s41558-021-01254-9, 2022.

Griffies, S. M., Danabasoglu, G., Durack, P. J., Adcroft, A. J., Balaji, V., Böning, C. W., Chassignet, E. P., Curchitser, E., Deshayes, J., Drange, H., Fox-Kemper, B., Gleckler, P. J., Gregory, J. M., Haak, H., Hallberg, R. W., Heimbach, P., Hewitt, H. T., Holland, D. M., Ilyina, T., Jungclaus, J. H., Komuro, Y., Krasting, J. P., Large, W. G., Marsland, S. J., Masina, S., McDougall, T. J., Nurser, A. J. G., Orr, J. C., Pirani, A., Qiao, F., Stouffer, R. J., Taylor, K. E., Treguier, A. M., Tsujino, H., Uotila, P., Valdivieso, M., Wang, Q., Winton, M., and Yeager, S. G.: OMIP contribution to CMIP6: experimental and diagnostic protocol for the physical component of the Ocean Model Intercomparison Project, Geosci. Model Dev., 9, 3231–3296, https://doi.org/10.5194/gmd-9-3231-2016, 2016.

Guerreiro, K., Fleury, S., Zakharova, E., Kouraev, A., Rémy, F., and Maisongrande, P.: Comparison of CryoSat-2 and ENVISAT radar freeboard over Arctic sea ice: toward an improved

Envisat freeboard retrieval, The Cryosphere, 11, 2059–2073, https://doi.org/10.5194/tc-11-2059-2017, 2017.

Haumann, F. A., Gruber, N., Münnich, M., Frenger, I., and Kern, S.: Sea-ice transport driving Southern Ocean salinity and its recent trends, Nature, 537, 89–92, https://doi.org/10.1038/nature19101, 2016.

Hersbach, H., Bell, B., Berrisford, P., Biavati, G., Horányi, A., Muñoz Sabater, J., Nicolas, J., Peubey, C., Radu, R., Rozum, I., Schepers, D., Simmons, A., Soci, C., Dee, D., and Thépaut, J.-N.: ERA5 hourly data on single levels from 1959 to present, Copernicus Climate Change Service (C3S) Climate Data Store (CDS) [data set], 10.24381/cds.adbb2d47, 2018.

Holland, P. R. and Kwok, R.: Wind-driven trends in Antarctic sea-ice drift, Nat. Geosci., 5, 872–875, https://doi.org/10.1038/ngeo1627, 2012.

Hu, A., Rooth, C., Bleck, R., and Deser, C.: NAO influence on sea ice extent in the Eurasian coastal region, Geophys. Res. Lett., 29, 10-1–10-4, https://doi.org/10.1029/2001gl014293, 2002.

Hunke, E. C. and Holland, M. M.: Global atmospheric forcing data for Arctic ice-ocean modeling, J. Geophys. Res.-Oceans., 112, C04S14, https://doi.org/10.1029/2006JC003640, 2007.

Hunke, E. C. and Lipscomb, W.: CICE: The Los Alamos sea ice model, documentation and software, version 4.0, Los Alamos National Laboratory, Technical Report LA-CC-06-012, 2008.

Hunke, E. C., Lipscomb, W. H., Turner, A. K., Jeffery, N., and Elliott, S.: CICE: the Los Alamos Sea Ice Model Documentation and Software User's Manual Version 5.1, Tech. Rep. LA-CC-06-012, Los Alamos National Laboratory, Los Alamos, New Mexico, USA, https://github.com/CICE-Consortium/CICE-svn-trunk/releases/tag/cice-5.1.2 (last access: 3 April 2023), 2015.

Kimura, N.: Sea ice motion in response to surface wind and ocean current in the Southern Ocean, J. Meteorol. Soc. Jpn., 82, 1223–1231, https://doi.org/10.2151/jmsj.2004.1223, 2004.

Kimura, N., Nishimura, A., Tanaka, Y., and Yamaguchi, H.: Influence of winter sea-ice motion on summer ice cover in the Arctic, Polar Res., 32, 20193, https://doi.org/10.3402/polar.v32i0.20193, 2013.

Komuro, Y., Suzuki, T., Sakamoto, T. T., Hasumi, H., Ishii, M., Watanabe, M., Nozawa, T., Yokohata, T., Nishimura, T., Ogochi, K., Emori, S., and Kimoto, M.: Sea-ice in twentieth-century simulations by new MIROC coupled models: a comparison between models with high resolution and with ice thickness distribution, J. Meteorol. Soc. Jpn., 90A, 213–232, 2012.

Krikken, F. and Hazeleger, W.: Arctic energy budget in relation to sea ice variability on monthly-to-annual time scales, J. Climate, 28, 6335–6350, https://doi.org/10.1175/JCLI-D-15-0002.1, 2015.

Kurtz, N. T. and Markus, T.: Satellite observations of Antarctic sea ice thickness and volume, J. Geophys. Res.-Oceans, 117, C08025, https://doi.org/10.1029/2012JC008141, 2012.

Large, W. G. and Yeager, S. G.: The global climatology of an interannually varying air-sea flux data set, Clim. Dynam., 33, 341–364, https://doi.org/10.1007/s00382-008-0441-3, 2009.

Lavergne, T., Sørensen, A. M., Kern, S., Tonboe, R., Notz, D., Aaboe, S., Bell, L., Dybkjær, G., Eastwood, S., Gabarro, C., Heygster, G., Killie, M. A., Brandt Kreiner, M., Lavelle, J., Saldo, R., Sandven, S., and Pedersen, L. T.: Version 2 of the EUMETSAT OSI SAF and ESA CCI sea-ice concentration climate data records, The Cryosphere, 13, 49–78, https://doi.org/10.5194/tc-13-49-2019, 2019.

Lecomte, O., Goosse, H., Fichefet, T., Holland, P. R., Uotila, P., Zunz, V., and Kimura, N.: Impact of surface wind biases on the Antarctic sea ice concentration budget in climate models, Ocean Model., 105, 60–70, https://doi.org/10.1016/j.ocemod.2016.08.001, 2016.

Lindsay, R., Wensnahan, M., Schweiger, A., and Zhang, J.: Evaluation of seven different atmospheric reanalysis products in the Arctic, J. Climate, 27, 2588–2606, https://doi.org/10.1175/JCLI-D-13-00014.1, 2014.

Lin, X., Zhai, X., Wang, Z., and Munday, D. R.: Mean, variability, and trend of Southern Ocean wind stress: Role of wind fluctuations, J. Climate, 31, 3557–3573, https://doi.org/10.1175/JCLI-D-17-0481.1, 2018.

Lin, X., Massonnet, F., Fichefet, T., and Vancoppenolle, M.: SITool (v1.0) – a new evaluation tool for large-scale sea ice simulations: application to CMIP6 OMIP, Geosci. Model Dev., 14, 6331–6354, https://doi.org/10.5194/gmd-14-6331-2021, 2021.

Mahlstein, I., Gent, P. R., and Solomon, S.: Historical Antarctic mean sea ice area, sea ice trends, and winds in CMIP5 simulations, J. Geophys. Res.-Atmos., 118, 5105–5110, https://doi.org/10.1002/jgrd.50443, 2013.

Massonnet, F., Fichefet, T., Goosse, H., Vancoppenolle, M., Mathiot, P., and König Beatty, C.: On the influence of model physics on simulations of Arctic and Antarctic sea ice, The Cryosphere, 5, 687–699, https://doi.org/10.5194/tc-5-687-2011, 2011.

Massonnet, F., Fichefet, T., Goosse, H., Bitz, C. M., Philippon-Berthier, G., Holland, M. M., and Barriat, P.-Y.: Constraining projections of summer Arctic sea ice, The Cryosphere, 6, 1383–1394, https://doi.org/10.5194/tc-6-1383-2012, 2012.

Mellor, G. L. and Kantha, L.: An ice-ocean coupled model, J. Geophys. Res., 94, 10937–10954, https://doi.org/10.1029/JC094iC08p10937, 1989.

Meneghello, G., Marshall, J., Campin, J. M., Doddridge, E., and Timmermans, M. L.: The Ice-Ocean Governor: Ice-Ocean Stress Feedback Limits Beaufort Gyre Spin-Up, Geophys. Res. Lett., 45, 11293–11299, https://doi.org/10.1029/2018GL080171, 2018.

Notz, D. and SIMIP Community: Arctic Sea Ice in CMIP6, Geophys. Res. Lett., 47, 1–11, https://doi.org/10.1029/2019GL086749, 2020.

Notz, D., Jahn, A., Holland, M., Hunke, E., Massonnet, F., Stroeve, J., Tremblay, B., and Vancoppenolle, M.: The CMIP6 Sea-Ice Model Intercomparison Project (SIMIP): understanding sea ice through climate-model simulations, Geosci. Model Dev., 9, 3427–3446, https://doi.org/10.5194/gmd-9-3427-2016, 2016.

Olason, E. and Notz, D.: Drivers of variability in Arctic sea-ice drift speed, J. Geophys. Res.-Oceans, 119, 5755–5775, https://doi.org/10.1002/2014JC009897, 2014.

Parkinson, C. L.: A 40-y record reveals gradual Antarctic sea ice increases followed by decreases at rates far exceeding the rates seen in the Arctic, P. Natl. Acad. Sci. USA, 116, 14414–14423, https://doi.org/10.1073/pnas.1906556116, 2019.

Rampal, P., Weiss, J., Dubois, C., and Campin, J. M.: IPCC climate models do not capture Arctic sea ice drift acceleration: Consequences in terms of projected sea ice thinning and decline, J. Geophys. Res.-Oceans, 116, C00D07, https://doi.org/10.1029/2011JC007110, 2011.

Raphael, M. N. and Hobbs, W.: The influence of the large-scale atmospheric circulation on Antarctic sea ice during ice advance and retreat seasons, Geophys. Res. Lett., 41, 5037–5045, https://doi.org/10.1002/2014GL060365, 2014.

Raphael, M. N. and Handcock, M. S.: A new record minimum for Antarctic sea ice, Nat. Rev. Earth Environ., 3, 215–216, https://doi.org/10.1038/s43017-022-00281-0, 2022.

Renwick, J. A., Kohout, A., and Dean, S.: Atmospheric forcing of Antarctic sea ice on intraseasonal time scales, J. Climate, 25, 5962–5975, https://doi.org/10.1175/JCLI-D-11-00423.1, 2012.

Rigor, I. G., Wallace, J. M., and Colony, R. L.: Response of sea ice to the Arctic Oscillation, J. Climate, 15, 2648–2663, https://doi.org/10.1175/1520-0442(2002)015<2648:ROSITT>2.0.CO;2, 2002.

Roach, L. A., Dörr, J., Holmes, C. R., Massonnet, F., Blockley, E. W., Notz, D., Rackow, T., Raphael, M. N., O'Farrell, S. P., Bailey, D. A., and Bitz, C. M.: Antarctic Sea Ice Area in CMIP6, Geophys. Res. Lett., 47, 1–10, https://doi.org/10.1029/2019GL086729, 2020.

Rosenblum, E. and Eisenman, I.: Sea ice trends in climate models only accurate in runs with biased global warming, J. Climate, 30, 6265–6278, https://doi.org/10.1175/JCLI-D-16-0455.1, 2017.

Rousset, C., Vancoppenolle, M., Madec, G., Fichefet, T., Flavoni, S., Barthélemy, A., Benshila, R., Chanut, J., Levy, C., Masson, S., and Vivier, F.: The Louvain-La-Neuve sea ice model LIM3.6: global and regional capabilities, Geosci. Model Dev., 8, 2991–3005, https://doi.org/10.5194/gmd-8-2991-2015, 2015.

Seland, Ø., Bentsen, M., Olivié, D., Toniazzo, T., Gjermundsen, A., Graff, L. S., Debernard, J. B., Gupta, A. K., He, Y.-C., Kirkevåg, A., Schwinger, J., Tjiputra, J., Aas, K. S., Bethke, I., Fan, Y., Griesfeller, J., Grini, A., Guo, C., Ilicak, M., Karset, I. H. H., Landgren, O., Liakka, J., Moseid, K. O., Nummelin, A., Spensberger, C., Tang, H., Zhang, Z., Heinze, C., Iversen, T., and Schulz, M.: Overview of the Norwegian Earth System Model (NorESM2) and key climate response of CMIP6 DECK, historical, and scenario simulations, Geosci. Model Dev., 13, 6165–6200, https://doi.org/10.5194/gmd-13-6165-2020, 2020.

Sévellec, F., Fedorov, A. V., and Liu, W.: Arctic sea-ice decline weakens the Atlantic Meridional Overturning Circulation, Nat. Clim. Change, 7, 604–610, https://doi.org/10.1038/NCLIMATE3353, 2017.

Shu, Q., Song, Z., and Qiao, F.: Assessment of sea ice simulations in the CMIP5 models, The Cryosphere, 9, 399–409, https://doi.org/10.5194/tc-9-399-2015, 2015.

Shu, Q., Wang, Q., Song, Z., Qiao, F., Zhao, J., Chu, M., and Li, X.: Assessment of sea ice extent in CMIP6 with comparison to observations and CMIP5, Geophys. Res. Lett., 47, 1–9, https://doi.org/10.1029/2020GL087965, 2020.

Smith, D. M., Dunstone, N. J., Scaife, A. A., Fiedler, E. K., Copsey, D., and Hardiman, S. C.: Atmospheric response to Arctic and Antarctic sea ice: The importance of ocean-atmosphere coupling and the background state, J. Climate, 30, 4547–4565, https://doi.org/10.1175/JCLI-D-16-0564.1, 2017.

Smith, D. M., Eade, R., Andrews, M. B., Ayres, H., Clark, A., Chripko, S., Deser, C., Dunstone, N. J., García-Serrano, J., Gastineau, G., Graff, L. S., Hardiman, S. C., He, B., Hermanson, L., Jung, T., Knight, J., Levine, X., Magnusdottir, G., Manzini, E., Matei, D., Mori, M., Msadek, R., Ortega, P., Peings, Y., Scaife, A. A., Screen, J. A., Seabrook, M., Semmler, T., Sig-

mond, M., Streffing, J., Sun, L., and Walsh, A.: Robust but weak winter atmospheric circulation response to future Arctic sea ice loss, Nat. Commun., 13, 1–15, https://doi.org/10.1038/s41467-022-28283-y, 2022.

Sterlin, J., Fichefet, T., Massonnet, F., Lecomte, O., and Vancoppenolle, M.: Sensitivity of Arctic sea ice to melt pond processes and atmospheric forcing: A model study, Ocean Model., 167, 101872, https://doi.org/10.1016/j.ocemod.2021.101872, 2021.

Stroeve, J. and Notz, D.: Changing state of Arctic sea ice across all seasons, Environ. Res. Lett., 13, 103001, https://doi.org/10.1088/1748-9326/aade56, 2018.

Stroeve, J., Barrett, A., Serreze, M., and Schweiger, A.: Using records from submarine, aircraft and satellites to evaluate climate model simulations of Arctic sea ice thickness, The Cryosphere, 8, 1839–1854, https://doi.org/10.5194/tc-8-1839-2014, 2014.

Stroeve, J., Holland, M. M., Meier, W., Scambos, T., and Serreze, M.: Arctic sea ice decline: Faster than forecast, Geophys. Res. Lett., 34, 1–5, https://doi.org/10.1029/2007GL029703, 2007.

Tandon, N. F., Kushner, P. J., Docquier, D., Wettstein, J. J., and Li, C.: Reassessing sea ice drift and its relationship to long-term Arctic sea ice loss in coupled climate models, J. Geophys. Res.-Oceans, 123 4338–4359, https://doi.org/10.1029/2017JC013697, 2018.

Tatebe, H., Ogura, T., Nitta, T., Komuro, Y., Ogochi, K., Takemura, T., Sudo, K., Sekiguchi, M., Abe, M., Saito, F., Chikira, M., Watanabe, S., Mori, M., Hirota, N., Kawatani, Y., Mochizuki, T., Yoshimura, K., Takata, K., O'ishi, R., Yamazaki, D., Suzuki, T., Kurogi, M., Kataoka, T., Watanabe, M., and Kimoto, M.: Description and basic evaluation of simulated mean state, internal variability, and climate sensitivity in MIROC6, Geosci. Model Dev., 12, 2727–2765, https://doi.org/10.5194/gmd-12-2727-2019, 2019.

Tschudi, M., Meier, W. N., Stewart, J. S., Fowler, C., and Maslanik, J.: Polar Pathfinder Daily 25 km EASE-Grid Sea Ice Motion Vectors, Version 4.1, Boulder, Colorado USA, NASA National Snow and Ice Data Center Distributed Active Archive Center [data set], https://doi.org/10.5067/INAWUWO7QH7B, 2019.

Tsujino, H., Motoi, T., Ishikawa, I., Hirabara, M., Nakano, H., Yamanaka, G., Yasuda, T., and Ishizaki, H.: Reference manual for the Meteorological Research Institute Community Ocean Model (MRI.COM) Version 3, Technical Report of the Meteorological Research Institute, 59, 241, https://doi.org/10.11483/mritechrepo.59, 2010.

Tsujino, H., Urakawa, S., Nakano, H., Small, R. J., Kim, W. M., Yeager, S. G., Danabasoglu, G., Suzuki, T., Bamber, J. L., Bentsen, M., Böning, C. W., Bozec, A., Chassignet, E. P., Curchitser, E., Boeira Dias, F., Durack, P. J., Griffies, S. M., Harada, Y., Ilicak, M., Josey, S. A., Kobayashi, C., Kobayashi, S., Komuro, Y., Large, W. G., Le Sommer, J., Marsland, S. J., Masina, S., Scheinert, M., Tomita, H., Valdivieso, M., and Yamazaki, D.: JRA-55 based surface dataset for driving ocean-sea-ice models (JRA55-do), Ocean Model., 130, 79–139, https://doi.org/10.1016/j.ocemod.2018.07.002, 2018.

Tsujino, H., Urakawa, L. S., Griffies, S. M., Danabasoglu, G., Adcroft, A. J., Amaral, A. E., Arsouze, T., Bentsen, M., Bernardello, R., Böning, C. W., Bozec, A., Chassignet, E. P., Danilov, S., Dussin, R., Exarchou, E., Fogli, P. G., Fox-Kemper, B., Guo, C., Ilicak, M., Iovino, D., Kim, W. M., Koldunov, N., Lapin, V., Li, Y., Lin, P., Lindsay, K., Liu, H., Long, M. C., Komuro,

Y., Marsland, S. J., Masina, S., Nummelin, A., Rieck, J. K., Ruprich-Robert, Y., Scheinert, M., Sicardi, V., Sidorenko, D., Suzuki, T., Tatebe, H., Wang, Q., Yeager, S. G., and Yu, Z.: Evaluation of global ocean–sea-ice model simulations based on the experimental protocols of the Ocean Model Intercomparison Project phase 2 (OMIP-2), Geosci. Model Dev., 13, 3643–3708, https://doi.org/10.5194/gmd-13-3643-2020, 2020.

Turner, J., Bracegirdle, T. J., Phillips, T., Marshall, G. J., and Scott Hosking, J.: An initial assessment of Antarctic sea ice extent in the CMIP5 models, J. Climate, 26, 1473–1484, https://doi.org/10.1175/JCLI-D-12-00068.1, 2013.

Uotila, P., Holland, P., Vihma, T., Marsland, S., and Kimura, N.: Is realistic Antarctic sea-ice extent in climate models the result of excessive ice drift?, Ocean Modell., 79, 33–42, https://doi.org/10.1016/j.ocemod.2014.04.004, 2014.

Watts, M., Maslowski, W., Lee, Y. J., Kinney, J. C., and Osinski, R.: A spatial evaluation of Arctic sea ice and regional limitations in CMIP6 historical simulations, J. Climate, 34, 6399–6420, https://doi.org/10.1175/JCLI-D-20-0491.1, 2021.

Wu, Y., Wang, Z., Liu, C., and Lin, X.: Impacts of high-frequency atmospheric forcing on Southern Ocean circulation and Antarctic sea ice, Adv. Atmos. Sci., 37, 515–531, https://doi.org/10.1007/s00376-020-9203-x, 2020.

Yi, D. and Zwally H. J.: Arctic Sea Ice Freeboard and Thickness, Version 1, (2003–2007), Boulder, Colorado USA, NASA National Snow and Ice Data Center Distributed Active Archive Center [data set], https://doi.org/10.5067/SXJVJ3A2XIZT, 2009.

Yukimoto, S., Kawai, H., Koshiro, T., Oshima, N., Yoshida, K., Urakawa, S., Tsujino, H., Deushi, M., Tanaka, T., Hosaka, M., Yabu, S., Yoshimura, H., Shindo, E., Mizuta, R., Obata, A., Adachi, Y., and Ishii, M.: The meteorological research institute Earth system model version 2.0, MRI-ESM2.0: Description and basic evaluation of the physical component, J. Meteorol. Soc. Jpn., 97, 931–965, https://doi.org/10.2151/jmsj.2019-051, 2019.

Zunz, V., Goosse, H., and Massonnet, F.: How does internal variability influence the ability of CMIP5 models to reproduce the recent trend in Southern Ocean sea ice extent?, The Cryosphere, 7, 451–468, https://doi.org/10.5194/tc-7-451-2013, 2013.